DNMT1-Mediated Regulation of Inhibitory Interneuron Migration Impacts Cortical Architecture and Function

Julia Reichard[1, 2], Philip Wolff[1], Jian Du[1], Camila L. Fullio[3,4], Lilli Dorp[1], Can Bora Yildiz[1,2], Jenice Linde[1,2], Johanna Vollmer[1], Shirley Kempf[1], Severin Graff[2,5], Gerion Nabbefeld[2,6], Minali Singh[7], Chao-Chung Kuo[8], K. Naga Mohan[7], Tanja Vogel[3], Simon Musall[2,5] and Geraldine Zimmer-Bensch[1, 2]

Affiliations

[1] RWTH Aachen University, Division of Neuroepigenetics, Institute of Zoology (Biology 2), Worringerweg 3, 52074 Aachen, Germany.

[2] Research Training Group 2416 Multi Senses – Multi Scales, RWTH Aachen University, 52074 Aachen, Germany

[3] Institute for Anatomy and Cell Biology, Department of Molecular Embryology, Faculty of Medicine, Albert-Ludwigs-University Freiburg, 79104 Freiburg, Germany

[4] Faculty of Biology, Albert-Ludwigs-University Freiburg, 79104 Freiburg, Germany

[5] Institute of Biological Information Processing (IBI-3) Bioelectronics, Forschungszentrum Jülich, Germany

[6] RWTH Aachen University, Division of Neurophysiology, Institute of Zoology (Biology 2), Worringerweg 3, 52074 Aachen, Germany.

[7] Molecular Biology and Genetics Laboratory, Department of Biological Sciences, BITS Pilani, Hyderabad Campus, Hyderabad, India

[8] Genomics Facility, Interdisciplinary Center for Clinical Research (IZKF), RWTH Aachen University, 52074 Aachen, Germany

Abstract

The fine-tuned establishment of neuronal circuits during the formation of the cerebral cortex is pivotal for its functionality. Developmental abnormalities affecting the composition of cortical circuits, which consist of excitatory neurons and inhibitory interneurons, are linked to a spectrum of neuropsychiatric disorders. Excitatory neurons originate in cortical proliferative zones, while inhibitory interneurons migrate from discrete domains of the basal telencephalon into the cortex. This migration is intricately governed by intrinsic genetic programs and extrinsic cues. Our current study reveals the role of the DNA methyltransferase 1 (DNMT1) in controlling expression of key genes implicated in mouse cortical interneuron development and in guiding the migration of somatostatin-expressing interneurons within the developing cortex. *Dnmt1* deletion causes interneurons to exit prematurely from the superficial migratory stream. In addition to the perturbed migration pattern and altered gene expression signatures, *Dnmt1*-deficient interneurons had a discernible non-cell autonomous effect on cortical progenitors, which culminated in nuanced alterations of layer thicknesses in the adult cortex. Our study reveals that an epigenetic mechanism governs the migration of cortical interneurons and through this, their instructive role in sculpting the intricate cortical layer architecture by signaling to cortical progenitors, with pronounced effects on cortical network function.

Introduction

The intricate neuronal circuitry of the mammalian cerebral cortex, composed of excitatory and inhibitory neurons, empowers its enormous cognitive capabilities. The circuit formation involves coordinated developmental steps: proliferation, differentiation, migration, morphological maturation, and synapse formation[1].

Excitatory cortical projection neurons originate from radial glial cells (RGCs) and intermediate progenitors (IPCs) located in the cortical proliferative zones, through direct and indirect neurogenesis. Symmetric divisions of RGCs initially expand the progenitor pool, later shifting to asymmetric divisions to produce neurons and RGCs or IPCs [2;3]. EOMES-expressing IPCs localize to the subventricular zone (SVZ) and divide into neurons for all cortical layers after few self-renewal divisions[3]. Cortical excitatory neurons are produced in a temporally regulated manner, with early-born neurons forming deep layers and later-born neurons forming superficial layers, coming with unique functional features and connectivity[4]. The timing of cortical neuron generation seems to be regulated by both intrinsic and extrinsic factors[2;3]. Intrinsic factors include (epi)genetic programs within progenitor cells that dictate their developmental potential. Extrinsic factors encompass signaling molecules from neighboring cells, postmitotic cells in the cortical plate, embryonic cerebrospinal fluid secreted by the choroid plexus, and incoming thalamic afferents[5–9]. These signals influence the self-renewal and neurogenic potential of cortical progenitors, ensuring the proper temporal patterning and layering of the cortex.

Despite composing only 10-20% of the neuronal population, cortical inhibitory neurons (cINs), including parvalbumin (PV) and somatostatin (SST) interneuron subtypes, crucially modulate cortical activity by inhibiting both excitatory and other inhibitory neurons, shaping cortical circuits for precise information processing[10]. Disruptions in their development unbalance excitation and inhibition, causing abnormal cortical activity and cognitive impairments in various neurological and neuropsychiatric disorders, such as schizophrenia or epilepsy[11–14]. The different types of cINs originate in three subpallial structures: the medial ganglionic eminence (MGE), the caudal ganglionic eminence (CGE), and the preoptic area (POA)[10]. The MGE gives rise to PV^+ and SST^+ interneurons, whereas the CGE generates Serotonin 3A receptor (5HTR3a) subtypes[15,16]. The POA produces mostly neurogliaform cells and Neuropeptide Y (NPY) expressing multipolar interneurons[17,18]. Postmitotic cINs migrate tangentially through the basal telencephalon into the cortex, guided by various extrinsic cues[19–22]. They invade the cortex along the marginal zone (MZ) and subventricular zone (SVZ)/intermediate zone (IZ), where they spread tangentially before switching to radial migration to enter the cortical plate. This migration pattern is under the influence of a diverse set of intrinsic and extrinsic cues[12]. For example, the transcription factors ARX and LHX6, expressed in MGE-derived interneurons, directly and indirectly regulate the expression of cytokine receptors that mediate the attraction to CXCL12, which is expressed in the MZ migratory route of the developing cortex[23,24]. After tangentially spreading over the cortical areas, cINs invade the cortical plate. The cortical plate expresses NRG2, which exerts attractive effects on ERBB4-expressing interneurons[25].

Epigenetic mechanisms, including histone modifications and DNA methylation, modulate intrinsic transcriptional programs[14,26]. It was previously reported that the DNA methyltransferase 1 (DNMT1) regulates gene expression programs in POA-derived cINs, promoting their proper migration and survival[27] through non-canonical interactions with histone

modifications[27]. MGE-derived cINs, which give rise to SST+ and PV+ interneuron subtypes also express DNMT1[27]. However, DNMT1 function in these cIN subsets is unknown so far. SST-expressing interneurons constitute about 30% of all cINs and play vital roles in inhibitory control, network synchronization, circuit plasticity, and cognitive functions[28]. SST+ cINs encompass two main subtypes: Martinotti cells, which migrate along the marginal zone (MZ) and form axon collaterals in layer I, and non-Martinotti cells, which disperse via the subventricular/intermediate zones (SVZ/IZ) and have different layer distributions as well as targeting properties[12,28]. Expression of transcription factors, including ARX, LHX6, and MAFB, correlates with the two different migratory paths[23,29,30]. MAFB marks Martinotti cells, mediating together with ARX[23] and LHX6[29] the migration of cINs along the MZ[30]. The migration of SST+ cINs along the MZ is linked to the axonal arbor formation in layer I[30]. Despite the critical roles of SST+ interneurons in cortical circuitry and their likely reliance on epigenetic regulation for proper development, the specific mechanisms by which DNMT1 influences SST+ cIN migration and its subsequent impact on cortical structure and function remain poorly understood. Additionally, given the temporally and spatially orchestrated migration patterns of SST+ cINs within the cortex, it remains unclear how the migration of this subpopulation might influence the proliferation and differentiation of cortical progenitors. Addressing this gap will help to understand how cell type-specific epigenetic regulation orchestrates the precise formation of cortical networks.

Recognizing the functional relevance of SST+ cINs, we here investigated the role of DNMT1 in their development. We found that reduced *Dnmt1* expression in SST+ interneurons altered the transcriptional and DNA methylation profiles of key genes for cIN development such as *Arx*. Thereby, *Dnmt1* deletion altered cIN migration along the MZ in the developing cortex. This impacted on the excitatory cortical progenitor pool and neurogenesis at specific developmental stages, and led to changes in cortical layering, functionality, and behavioral abnormalities in adulthood.

Results

DNMT1 regulates the expression of key genes during SST+-cIN development

To examine the role of DNMT1 specifically in the SST-expressing subtypes of cINs, we created a conditional knockout mouse model (*Sst-Cre/tdTomato/Dnmt1 loxP*[2]) with *Dnmt1* deletion being induced by *Cre*-expression in post-mitotic SST+ interneurons primarily originating in the MGE[31]. *Sst-Cre/tdTomato* mice served as controls (**Extended Data Fig. E1a**). The validation of the mouse models is shown in **Extended Data Fig. E1b-h**. We first focused on embryonic day (E) 14.5, a critical time when extensive migration of SST+ cINs occurs through the basal telencephalon, marking the beginning of their invasion into the cerebral cortex[31]. To reveal putative target genes of DNMT1, we conducted RNA sequencing and methyl-sequencing of FACS-enriched E14.5 *Sst-Cre/tdTomato/Dnmt1 loxP*[2] and *Sst-Cre/tdTomato* cells, to determine changes in transcriptional and DNA methylation profiles, respectively. We found 1080 differentially expressed genes (DEGs) and 9919 differentially methylated sites (DMSs) in E14.5 *Dnmt1* deficient *Sst-Cre/tdTomato* cells (**Fig. 1a-c, Supplementary Table 1**). As differentially methylated regions (DMRs) encompass broader genomic regions, such as promoters, enhancers, and other regulatory elements[32,33], they often hold greater regulatory significance than single DMSs. To account for this, we also calculated DMRs, identifying a

total of 23622 regions. Correlating these DMRs to the DEGs, we identified 600 genes that exhibit both alterations in gene expression (up- and downregulation) and DNA methylation in *Sst-Cre/tdTomato/Dnmt1 loxP*[2] cells (**Fig. 1d, Supplementary Table 2 and 3**). 349 of these 600 genes increased in expression upon *Dnmt1* deletion (**Fig. 1d**), pointing to putative targets of DNMT1-dependent repressive DNA methylation in SST$^+$ interneurons of control mice. In support of this, 66 of these 349 genes exhibited DNMT1 binding motifs that we have identified through additional ChIP-sequencing experiments (**Fig. 1d, g, Supplementary Table 4**).

Gene Ontology (GO) analysis on genes, which increased significantly in *Sst-Cre/Dnmt1* KO cells and concomitantly exhibited changes in DNA methylation, revealed a significant enrichment of genes that are functionally associated with nervous system development, neuron differentiation, cell-cell signaling, locomotion, neurogenesis, and cell differentiation (**Fig. 1f, Supplementary Table 5).** Similar results were observed for the entire set of significantly upregulated genes in *Dnmt1* KO samples, regardless of concurrent changes in DNA methylation (**Supplementary Table 6**). Notably, among the genes with altered expression and DNA methylation, we identified key regulators of cortical interneuron differentiation and maturation, such as *Arx*, *Zeb*, *Mef2c*, *Dlx1*, *Sox6*, *Mafb*, and *Lhx6*. In addition to these well-known transcription factors that govern cIN fate and development[12,31,34], we found locomotion and cell-cell signaling-related genes to be regulated by DNMT1 (**Fig. 1b, f, h**). These included *Erbb4*, *Sema3A*, and *Robo2*, as well as members of the Eph/ephrin family such as *Efnb2*, which encode proteins that are crucial for directional guidance and neuronal positioning[25,35,36,37]. Of note, *Erbb4*, *Mafb*, *Arx*, *Lhx6,* and *Sox6,* were amongst the most highly differentially expressed genes compared to controls (**Fig. 1a, b**). This positions DNMT1 as a crucial epigenetic regulator of these key genes in cIN development. Moreover, these genes along with numerous others that upregulated upon *Dnmt1* deletion in E14.5 SST$^+$ cINs, were downregulated in embryonic stem cell (ESC)-derived *Dnmt1*$^{tet/tet}$ neurons that overexpressed *Dnmt1* (**Supplementary Table 6**). In general, a significant proportion of all differentially expressed genes upon *Dnmt1* deletion in E14.5 SST$^+$ interneurons (up- and downregulated), were also dysregulated in an opposite direction in these neurons overexpressing DNMT1 (**Fig. 1e, Supplementary Table 6, 7**).

Remarkably, the DNMT1-regulated gene sets displayed significantly longer coding sequences, transcript lengths, genome spans as well as lengths of the 3´UTRs and 5`UTRs compared to the whole set of genes that were detected in SST$^+$ cINs. Moreover, compared to the reference gene list of all detected transcripts, DNMT1-dependent DEGs contained significantly more protein-coding genes, as well as exons and isoforms (*Chi-squared test*; **Extended Data Fig. E2, E3, E4, E6**). Many genes involved in neuronal function and development are known to be particularly long[38], further supporting our finding that DNMT1-dependent DNA methylation regulates key neurodevelopmental genes **(Fig. 1a, f, Supplementary Table 1-7)**. In line with this, the deletion of MeCP2, a reader of DNA methylation[39], also results in the upregulation of such long genes[38].

Dnmt1 deletion in SST$^+$ interneurons resulted in differentially methylated sites near transcriptional start sites (TSS) as well as within intragenic regions and intergenic loci (**Figure 1i**, **Supplementary Table 2**, **Extended Data Fig. E4**). Intragenic DNA methylation associates with alternative promoter choice and alternative splicing, while DNA methylation at promoter regions represses transcription[40]. We therefore plotted changes in DNA methylation for the aforementioned key genes of interneuron development at the TSS due to its well-documented

181 impact on gene transcription (**Fig. 1i**). Consistent with previous studies[27,41], we observed sites
182 with decreased and increased CpG methylation in *Dnmt1* deficient interneurons, also in
183 specific regions around the TSS (**Fig. 1i, Supplementary Table 2**, **Extended Data Fig. 4**).
184 These changes in DNA methylation aligned with genes that increased or decreased
185 significantly in expression in both *Dnmt1* knockout and in *Dnmt1* overexpressing neurons (**Fig.**
186 **1a-c, d, e**; **Supplementary Table 7**)[27,41].
187 For *Arx,* we detected strongly reduced DNA methylation at the TSS, as well as in up- and
188 downstream regions in *Sst-Cre*/*Dnmt1* KO samples (**Fig. 1i, j**), which correlated well with
189 increased *Arx* expression detected in *Sst-Cre*/*Dnmt1* KO cells. Moreover, the regions around
190 the TSS of *Zeb2* and *Sox6* displayed reduced methylation (**Fig. 1i**), two genes that also
191 increased significantly in expression (**Fig. 1a, b, h**). These genes encode proteins with key
192 roles in (SST$^+$) cIN development. ARX is crucial for cIN migration within the marginal zone
193 (MZ)[23], and SOX6 is required for the proper positioning of basket and Martinotti neurons[42].
194 ZEB2 promotes the differentiation and migration of cortical GABAergic interneurons[43,44].
195 Apart from these key transcription factors that orchestrate cIN differentiation and migration, we
196 observed elevated expression levels for *Erbb4* upon *Dnmt1* deletion **(Fig. 1a, b, i)**. Elevated
197 ERBB4 expression at protein level was confirmed by immunostaining in dissociated MGE cells
198 (E14.5) following 24-hour treatment with *Dnmt1* siRNA oligos (**Extended Data Fig. E6a-c)**.
199 ERBB4 mediates the invasion of cortical interneurons into the cortical plate upon activation
200 by its ligand Neuregulin (NRG3)[25], which is expressed within the cortical plate. Hence, we
201 hypothesized that DNMT1 contributed to the proper migration of SST$^+$ interneurons along the
202 cortical migratory streams and timing of the tangential to radial switch in migrating cIN by
203 limiting *Erbb4* expression levels.
204 In sum, these results strongly suggest that DNMT1 contributes to the establishment of proper
205 gene regulatory networks that direct the migration and differentiation of SST$^+$ interneurons.
206
207 ***Dnmt1* deletion in postmitotic SST$^+$ interneurons causes a premature exit from the**
208 **superficial migratory stream in the embryonic cortex**
209 To investigate the function of DNMT1 in the development of SST$^+$ cINs in more detail, we next
210 analyzed the migration of *Sst-Cre/tdTomato/Dnmt1 loxP^2* and *Sst-Cre/tdTomato* cells at
211 different embryonic stages. We initially focused on embryonic stage (E)14.5, when first SST$^+$
212 interneurons have reached the cerebral cortex (**Fig. 2a-e**, **Extended Data Fig. E6d, e**). In situ
213 examination of *tdTomato*-expressing cells in coronal brain sections from E14.5 revealed
214 overall comparable numbers of SST$^+$ cINs across the cortex and within the basal
215 telencephalon in both genotypes (**Fig. 2b-e**). Yet, we observed a marked reduction of SST
216 interneurons within the marginal zone (MZ) in conditional *Dnmt1* knockout embryos, while the
217 proportion of *Sst-Cre/tdTomato/Dnmt1 loxP^2* neurons within the cortical plate was significantly
218 increased (**Fig. 2f-h**). To ensure the comparability of the two genotypes and to exclude slight
219 age differences, we also analyzed the dimensions of all brain sections, which revealed no
220 variations (**see Extended Data Fig. E7**). Live-cell imaging of organotypic brain slices at E14.5
221 for 20 hours revealed an increased proportion of *Dnmt1*-deficient SST$^+$ interneurons that
222 deviated from the superficial migratory stream and entered the cortical plate (CP; **Fig. 2i-k, o**
223 **and p, Supplementary Movies 1 and 2**), which aligned with the in situ observations (**Fig. 2f-**
224 **h**). Notably, *Dnmt1*-deficient SST$^+$ interneurons displayed a significantly increased frequency
225 of directional changes during their cortical migration (**Fig. 2l**), suggesting a disruption in their

ability to remain confined within the MZ stream. Moreover, their migratory pace was enhanced, which was particularly evident for radially migrating cells, and cells migrating through the cortical plate **(Fig. 2m-p**). This aligns with an increased path length seen for the migrating KO cells in the living brain slices (**Extended Data Fig. E6d, e**). Of note, in contrast to *Dnmt1*-deficient POA-derived *Hmx3*-expressing interneurons[27], we did not observe morphological abnormalities for migrating *Sst-Cre/tdTomato/Dnmt1 loxP*[2] cells (see **Extended Data Fig. E6f**). This aligns with in vitro experiments aiming to assess the morphology of *Dnmt1* siRNA-treated MGE cells (E14.5 +1div), in which we did not detect morphological differences compared to control transfections (**Extended Data Fig. E6g-i**). In combination with the sequencing data, our results point to a DNMT1-dependent regulation of SST$^+$ interneuron migration by ensuring their proper movement along the superficial stream along the MZ of the cortex. MZ migrating Martinotti cINs express distinct sets of genes compared to the SVZ migrating non-Martinotti cells[30]. SVZ cells show strong expression of e.g. *Sox1*, *Npy, Sp9, Tox,* and *Gabra2*, which in turn are repressed in MZ cells[30]. Moreover, *Erbb4* expression was recently described to be expressed in non-Martinotti cells[45]. Interestingly, we found these genes to be repressed by DNMT1 in SST$^+$ cINs **(Supplementary** Table 1). This proposes that DNMT1 mainly influences the migration of Martinotti cells.

Although *Dnmt1* KO SST$^+$ interneurons prematurely exited the superficial migratory stream and entered the cortical plate by E14.5 within 20 hours (**Fig. 2i-k**, **o and p**), we did not observe significant differences at later stages (E16.5 and E18.5). This was neither the case for the proportion of cells that reached the cortex nor for the absolute number, density, or distribution of *Sst-Cre/Dnmt1* KO cells within the cortical regions quantified (**Fig. 3**). The cortical dimensions were likewise similar between knockout and wildtype E16.5 and E18.5 embryos (**Extended Data Fig. E8**), confirming that the embryos analyzed were at comparable developmental stages. This suggests that the impact of *Dnmt1* deletion on the directional migration of SST$^+$ interneurons within the MZ may be transient.

DNMT1-dependent regulation of SST$^+$ interneuron migration affects cortical progenitors non-cell autonomously

The development of cIN and cortical excitatory neurons is intricately linked[46,47], and supernumerary cINs in the IZ were already described to elicit altered IPC numbers impacting the generation of upper layer excitatory neurons[47]. Observing an altered migration pattern of SST$^+$ interneurons invading the cortical plate and proliferative zones prompted us to investigate its influence on cortical progenitors and neurogenesis. Moreover, we found altered expression of genes involved in cell-cell signaling, known to modulate cortical neurogenesis, such as *efnB2*[48]. EphrinB2 can bind to EPHA4[49], being expressed by RGCs[5]. Activation of EPHA4 receptors by ephrinA5, expressed in invading thalamic afferents, has been shown to regulate RGC division, impacting cortical layer formation[5]. The premature exit from the superficial marginal stream in combination with altered expression of signaling molecules in *Sst-Cre/tdTomato/Dnmt1 loxP*[2] could therefore alter cell-cell signaling between interneurons and cortical progenitors, potentially affecting neurogenesis.

To investigate this question, we employed immunostaining for TBR1, labeling early-born neurons of the preplate and layer VI[50,51], to assess whether the generation of these neurons is

altered in *Sst-Cre/tdTomato/Dnmt1 loxP*[2] embryos. Indeed, we found a significant increase in TBR1$^+$ cells within the cortical plate (CP) in E14.5 *Sst-Cre/Dnmt1* KO embryos (**Fig. 4 b, c**), which became even more evident at E16.5 (**Fig. 4f, g**). At E18.5 the radial extension of both layer VI (TBR1+ cells) and the remaining CP were significantly expanded in the conditional *Dnmt1* KO embryos compared to age-matched controls (**Fig. 4j-m**). EOMES$^+$ IPCs represent an intermediate progenitor stage from RGCs to neurons, proposed to give rise to most cortical projection neurons of all cortical layers[52;53,54]. Altered cIN numbers in the embryonic cortex have already been reported to induce altered numbers of IPCs[47]. In line with that, we detected increased numbers of EOMES$^+$ IPCs at E14.5 in *Dnmt1* deficient animals, aligning temporally with the premature exit of *Dnmt1*-deficient SST interneurons from the MZ and the increased numbers of TBR1$^+$ neurons (**Fig. 4d, e**).
As no differences in the pool of IPCs were detected at E18.5 (**Fig. 4h, i**), the deletion of *Dnmt1* therefore seems to elicit a temporally restricted non-cell autonomous effect on cortical IPCs and the production of deep-layer neurons.

***Dnmt1*-deficient SST$^+$ interneurons display changes in transcription of genes known to modulate cortical progenitors**

The non-cell autonomous effect of *Dnmt1* deletion in SST$^+$ cINs on cortical progenitors and the generation of deep-layer neurons suggested, that cINs provide signaling molecules that act on cortical progenitors, similar to what was reported for thalamic afferents that import ephrinA5, which influences IPC generation from RGCs through the EPHA4 receptor[5]. *Dnmt1* deficiency in SST$^+$ cINs altered the expression of diverse signaling molecules that are known to modulate cortical neurogenesis and progenitor division, including *Wnt7a*, *Notch1* and *Notch3*, *Robo2*, *efnB2* and *Sema3A* (**Supplementary Table 1**) [6,55,56;57].
To analyze in detail which signaling molecules play a role in potential interactions between embryonic cortical interneurons and cortical progenitors, we took advantage of the *CellChat* bioinformatic tool, which enables quantitative extraction of cell-cell communication networks from single cell (sc)RNA-sequencing datasets. We exploited scRNA sequencing data from the E14.5 dorsal telencephalon from control mice to predict key outgoing and incoming signals for SST$^+$ cINs and cortical progenitor communication. This analysis allowed to assess quantitatively the probability of ligand-receptor interactions between specific cell types, because each cell type exhibits distinct sets of ligands and receptors with varying strengths, indicating their role as signaling senders and receivers. The probabilities of ligand-receptor pairs predicted to mediate the communication between SST$^+$ cINs with apical progenitors (APs) as well as with IPCs at E14.5 are shown in **Fig. 4 n, o**. The highest probability for interactions between SST$^+$ cINs with both APs and IPCs was calculated for NRXN3 – NLGN1 signaling. *Nrxn3* was upregulated in E14.5 *Dnmt1*-deficient SST$^+$ interneurons (and displayed decreased transcript levels in *Dnmt1* overexpressing neurons; **Supplementary Table 1, 7**). In addition, EFNB2/EPHA4 signaling was predicted to occur between *efnB2* expressing SST$^+$ MGE-interneurons, and APs as well as IPCs at E14.5 (**Fig. 4 n-o**). *Efnb2* was also upregulated in E14.5 *Dnmt1*-deficient SST$^+$ interneurons and dysregulated in *Dnmt1* overexpressing neurons (Fig. 1h, **Supplementary Table 1, 7**). EFNB2 acts as a pro-neurogenic cue in the embryonic neocortex[48], and can interact with EPHA4 receptors[58]. EPHA4 is expressed by cortical RGCs and known to be activated by EFNA5, which is imported by thalamic afferents. This interaction regulates the AP division mode, and through this IPC generation and the

316 neuronal output for deep versus upper cortical neurons[5]. Interestingly, EFNB2-mediated
317 increase in neuronal production is temporally restricted to the mid-corticogenesis stage
318 (E15.5)[48]. As we observed a transient defect of MZ migrating *Dnmt1*-deficient SST$^+$
319 interneurons in the E14.5 cortex, and increased *efnB2* expression level in these cINs, we argue
320 that EFNB2 imported by SST$^+$ interneurons could contribute to the regulation of the timed
321 generation of cortical neurons. Thus, we hypothesized that the increased expression of *efnB2*
322 in *Dnmt1*-deficient SST$^+$ interneurons could lead to increased differentiation of APs towards
323 IPCs and TBR1$^+$ neurons at E14.5 and E16.5. To address this question, we performed a pair-
324 cell assay according to a previous study[5], stimulating E14.5 dissociated cortical neurons plated
325 at clonal density with recombinant ephrinB2-Fc or control-Fc protein for 24 h. Immunostaining
326 against nestin and β-III-tubulin was used to identify APs and postmitotic neurons, respectively[5]
327 **(Fig. 4p**). This assay confirmed an increased proportion of neurogenic RGC divisions upon
328 ephrinB2-Fc stimulation (**Fig. 4q**). Moreover, we analyzed whether ephrinB2-Fc stimulation
329 likewise impacts the generation of EOMES$^+$ IPCs from RGCs, by immunostaining against
330 nestin and EOMES. Similar to the increase in asymmetric neurogenic divisions of RGCs, we
331 observed an augmented proportion of IPC/RGC pairs (**Fig. 4r, s**). In sum, these results indicate
332 that ephrinB2-Fc treatment stimulates RGCs to asymmetrically divide into neurons and IPCs.
333 In summary, our results indicate an essential role for DNMT1 in the migration of SST$^+$
334 interneurons, regulating the expression of key genes orchestrating cIN development but also
335 genes related to cortical neurogenesis. *Dnmt1* deletion in SST$^+$ interneurons alters their
336 migration trajectory along the MZ causing a premature invasion into the cortical plate and of
337 the cortical IZ-VZ. Likely in conjunction with increased expression of pro-neurogenic factors,
338 the altered cIN migration seems to influence non-cell autonomously neural differentiation of
339 RGCs towards IPCs and deep-layer neurons.
340
341 ***Dnmt1* deletion-induced changes at embryonic stages manifest in an altered cortical**
342 **architecture at adult stages**
343 Finally, we investigated whether the DNMT1-related changes in SST$^+$ interneuron migration,
344 cortical progenitors and in deep layer neuron generation results in long-lasting structural
345 changes in the adult cortex. We therefore conducted a comparative analysis of the distribution,
346 density, and fate of *Sst-Cre/tdTomato* and *Sst-Cre/tdTomato/Dnmt1 loxP^2* interneurons in adult
347 mice. Immunohistochemistry in adult brain sections confirmed SST expression, and in addition
348 the co-expression of NPY and calretinin in *Sst-Cre/tdTomato* cells of both genotypes
349 (**Extended Data Fig. E9**), in line with other studies[59]. However, a difference between the
350 genotypes was observed for the proportion of SST$^+$ cINs co-expressing PV, which was
351 significantly increased in *Sst-Cre/tdTomato/Dnmt1 loxP^2* mice compared to controls (**Fig. 5a-**
352 **c**). This is in line with the elevated transcript levels of *Mef2c* found in E14.5 *Sst-*
353 *Cre/tdTomato/Dnmt1 loxP^2* cells (**Fig 1h**). MEF2C is essential for the development of PV$^+$
354 interneurons, as it initiates distinct transcriptional programs in immature PV$^+$ interneurons upon
355 settling within the cortex by opening the chromatin landscapes at PV-specific loci[60,61]. Of note,
356 *Mef2c* expression is driven by MAF and MAFB, which also increased in expression upon
357 *Dnmt1* deletion[62] (**Fig 1h**). Hence, by repressing *Maf* and *Mefc2* expression DNMT1 appears
358 to promote the fate of SST$^+$ cINs.
359

While the comparative analysis of *Sst-Cre/tdTomato* cIN numbers across all cortical layers revealed no major differences between the genotypes (**Fig. 5d-f**), cell density in the superficial cortical layers was significantly increased in *Sst-Cre/tdTomato/Dnmt1 loxP²* mice **(Fig. 5f)**. CUX1 immunostaining, labeling layer II-IV neurons, was utilized to discriminate between the superficial layers II-IV from deep layers V and VI **(Fig. 5d, e)**. This staining visualized a reduced radial extension of the CUX1-positive superficial layers II-IV in *Sst-Cre/tdTomato/Dnmt1 loxP²* mice **(Fig. 5g)**, explaining the increased SST^+ cIN densities **(Fig. 5f)**. In contrast, the deep layers V and VI were increased in their radial extension, while the overall cortical thickness did not differ between the knockout and control mice (**Fig. 5g**). This shift in the radial extension of the deep versus upper cortical layers is consistent with the increased numbers of TBR1 positive neurons observed at E14.5 and E16.5. These findings suggest that the non-cell autonomous effect of *Dnmt1* deletion in SST^+ interneurons on cortical progenitors and the timed neuronal production manifests in changes of the adult cortical architecture, which in turn affects SST^+-interneuron densities in the upper cortical layers.

Sst-Cre/tdTomato/Dnmt1 **KO mice display functional and behavioral abnormalities**

To analyze whether the observed structural changes in the adult cortex also translate into functional changes, we conducted high-density Neuropixels recordings in the primary somatosensory barrel cortex (S1) in awake head-fixed *Sst-Cre/tdTomato/Dnmt1 loxP²* and *Sst-Cre/tdTomato* control mice. Mice were placed on a running wheel during passive tactile stimulation, consisting of short air puffs to the whisker pad[63] (**Fig. 5h**). Neuropixels can simultaneously capture the single-cell activity of many neurons across the entire cortical depth, representing a powerful tool to investigate neural activity with high resolution and scale. Tactile stimulation induced a clear transient response in average local field potentials (LFPs) across all cortical layers of SST-Cre control mice. In contrast, LFP responses in conditional *Dnmt1* KO mice were much weaker and temporally delayed (**Fig. 5i, k**), suggesting a disruption in sensory processing. Moreover, LFP responses in *Sst-Cre/tdTomato/Dnmt1 loxP²* mice did not exhibit a positive rebound after the initial negative deflection, potentially due to a lack of feed-forward inhibition (**Fig. 5k**).

To better assess the spatiotemporal structure of synaptic inputs to the cortical column, we also employed a current source density (CSD) analysis[64] (**Fig. 5j**). The earliest responses for *Sst-Cre/tdTomato* mice (left) occurred in the granular layer at ~400 µm cortical depth and then spread to layer 2/3 (100-300 µm) and layer 5 (500-900 µm). These responses were in good agreement with the literature[65], suggesting intact spatiotemporal processing of sensory signals. In contrast, the CSD profile in *Sst-Cre/tdTomato/Dnmt1 loxP²* mice was strongly disrupted and showed no clear spatial pattern across cortical layers in response to tactile stimulation. These results strongly suggest that the DNMT1-related structural changes in the adult cortex also cause a marked disruption of cortical network function.

We next used spike-sorting to extract the spiking activity of cortical S1 neurons to quantify their temporal precision in response to tactile stimulation. Consistent with the LFP results, the peristimulus time histogram (PSTH) showed weaker spiking responses for all neurons that responded to the tactile stimulus in *Dnmt1* KO mice compared to control mice. This was particularly evident in the first neural response within 30 ms after sensory stimulation (**Fig. 5l**). Interestingly, sensory responses in *Dnmt1* KO mice were much longer lasting compared to control mice, with neural responses extending up to 400 ms after sensory stimulation **(Fig. 5l,**

m, o). As indicated by our LFP results, this could be due to a lack of SST-related feedback inhibition which prevented the overextended activation of excitatory neurons in control mice. Moreover, tactile spiking responses were also significantly broader in *Dnmt1* KO mice, shown by the full width at half maximum (FWHM) of the initial responses to sensory stimulation (**Fig. 5m**), again pointing to a reduction in the temporal precision of sensory processing in *Dnmt1* KO versus control mice.

To further test for functional changes in the adult cortex of *Dnmt1*-KO mice, we also measured neural responses to 5s-long visual grating stimuli in the primary visual cortex (V1, **Fig. 5p, q**). Visual stimulation increased neural activity and resulted in strong cortical network oscillations in the gamma range, especially around 30 Hz and 70 Hz (**Fig. 5q**). Such gamma (γ) oscillations from 30-120 Hz are essential for integrating neural networks within and across brain structures during cognitive processes, and strongly rely on accurate function of SST$^+$ cINs[66,67]. Abnormalities in γ oscillations are therefore a signature of dysfunction in neuronal networks and are often disturbed in cognitive diseases such as schizophrenia, Alzheimer´s disease and Fragile X syndrome[68].

Thus, changes in γ-oscillations represent a useful marker of function and dysfunction in cortical circuit operations[69]. In line with the impaired neural responses to tactile stimulation in S1, we found that gamma oscillations in *Dnmt1*-KO mice were strongly reduced, while responses in lower frequency bands were increased compared to control mice (**Fig. 5q**). These clear changes in cortical oscillations further demonstrate that DNMT1 deletion results in dysfunctional neural networks in the adult cortex, most likely due to an impairment of SST$^+$ cIN function and structural changes in cortical network architecture.

Based on these observations, we next asked whether behavioral outputs were altered correspondingly. Moreover, we noted abnormal eye movements during the tests on the running wheel (**Supplementary Video 3**), and frequent jumping of *Sst-Cre/tdTomato/Dnmt1 loxP^2* mice in their home cages (**Supplementary Video 4**). These behavioral abnormalities suggest defects related to neurological or neuropsychiatric diseases[70]. We additionally exploited the curated MGI function in ShinyGO, which enables insights into phenotypes, or disease associations linked to given gene sets. Analysis of the upregulated genes in *Dnmt1*-deficient SST$^+$ interneurons using the curated MGI function resulted in numerous terms related to behavioral abnormalities and seizure phenotypes (**Extended Data Fig. E9e).** Given the reported implication of cortical SST$^+$-interneuron dysfunction in various neuropsychiatric and neurological disorders, such as schizophrenia and autism spectrum disorders[71], we tested for disease-relevant behavior. We first scored nest-building performance, as defects in nest-building behavior can indicate general distress resulting from disease-related impairments[72]. In line with our functional results, we found that *Sst-Cre/tdTomato/Dnmt1 loxP^2* mice showed a reduced performance and diminished interest in nest-building material (**Fig.6a-e**). Furthermore, changes in SST$^+$ cIN activity and function have been reported to cause epileptic events[71], and γ oscillations are proposed to play a role in seizure generation[73]. Hence, we next conducted pharmacological interventions by administering PTZ (pentylenetetrazol), which is widely utilized to examine epilepsy in animal models and to assess changes in seizure responses[74]. Our findings revealed prolonged seizure durations for *Sst-Cre/tdTomato/Dnmt1* loxP^2 mice, which point to alterations in cortical inhibition (**Figure 6f-h**, Supplementary Videos 5-11).

In summary, our cellular, functional, and behavioral results demonstrate that *Dnmt1* deletion in postmitotic SST$^+$ interneurons leads to altered cortical architecture and network function in adult mice. This strongly suggests that DNMT1 plays a crucial role in the development of SST$^+$ interneurons and has non-cell autonomous functions essential for the proper formation of the cerebral cortex.

Discussion

Two novel and main features of cortical development arise from our experiments: (i) dispersion of SST$^+$ interneurons along the superficial migratory stream within the cortical MZ is regulated by DNMT1, and (ii) invading cortical interneurons influence apical cortical progenitors and through this proper cortical layering.

Dnmt1 deletion in SST-expressing interneurons caused a premature exit from the MZ at E14.5, accompanied by increased numbers of EOMES$^+$ IPCs at E14.5 and more TBR1-positive postmitotic neurons at E14.5 and E16.5, likely resulting from the altered division mode of RGCs. This led to an extended cortical plate at E18.5 and enlarged deep layers at adult stages, while upper layers were reduced in radial extension. These changes in cortical architecture and resulting altered densities of SST$^+$ interneurons in adult mice were associated with clear functional and behavioral deficits, demonstrating the importance of DNMT1 for establishing accurate network function in the adult cortex.

Martinotti cells constitute the majority of SST$^+$ interneurons and localize frequently in superficial layers II/III and deep layers V and VI[59]. They migrate primarily along the MZ during corticogenesis[30]. In contrast, non-Martinotti SST$^+$ cells disperse rather via the SVZ/IZ and express a distinct set of genes[30]. From the reported genes being distinctively expressed between SST$^+$ cells of the SVZ versus MZ migratory stream[30], we identified several genes to be regulated by DNMT1. For example, genes like *Sox1*, *Robo1* and *Npy*[30], which are expressed higher in SVZ-migrating SST$^+$ cells compared to ones migrating along the MZ, were repressed by DNMT1 in E14.5 SST$^+$ cINs (Supplementary Table S1). Moreover, *Erbb4* was reported as a marker gene for Martinotti SST$^+$ cells[45], being repressed by DNMT1 in SST$^+$ cells. In combination with the selective effects of *Dnmt1* deletion on MZ migrating SST$^+$ interneurons, these findings propose DNMT1 to be relevant for proper migration of Martinotti cells.

Apart from genes being distinctively expressed between MZ versus SVZ migrating SST$^+$ interneurons, our global transcriptome and methylome analyses propose that DNMT1 controls other essential key transcription factors of MGE-cortical interneuron development such as LHX6, ARX, ZEB2, SATB1, SOX1, SOX6, and DLX5[12,31,34]. ARX has been reported to directly and indirectly modulate other genes controlling different stages of cortical interneuron development, including *Maf*, *Mafb*, *Mef2c*, *Nkx2*.1, *Lmo1*, *Cxcr4*, *Nrg1*, *Erbb4*, *Sema3*, *Npr1*, and *EphA4*[23], many of which were altered in expression upon *Dnmt1* deletion in SST$^+$ interneurons. The elevated *Mef2c* levels in *Sst-Cre/tdTomato/Dnmt1 loxP*^{2} cells are in line with the increased proportion of PV-positive SST$^+$-tdTomato cells in adult *Dnmt1* KO mice, as Mef2c was reported to drive the PV fate[60,61]. In addition to ARX, MAF and MAFB promote *Mef2c* expression[62], which also increased in expression upon *Dnmt1* deletion.

In line with the observed transcriptional changes, *Lhx6*, *Maf, Mafb,* and *Arx* mutant mouse brains display a defect in cIN migration within the marginal zone (MZ)[23,29,30]. Moreover, ERBB4

494 regulates the switch from tangential to radial migration and the distribution of interneurons
495 within the CP. Tangential migration of cINs within the cortex is promoted by the CXCR4
496 receptor that binds to CXCL12, the latter being enriched in the MZ and SVZ migratory
497 streams[24]. The ERBB4 receptor recognizes NRG3, which is expressed in the CP, promoting
498 the radial navigation into the CP[25]. Both the loss of CXCR4 receptor in migrating interneurons,
499 and *Nrg3* overexpression in the CP result in premature invasion of migrating interneurons into
500 the CP[25]. As we did not detect an altered expression of *Cxcr4* in *Dnmt1*-deficient SST$^+$
501 interneurons, the increased *Erbb4* expression likely contributes to the premature invasion of
502 the CP in *Sst-Cre/tdTomato/Dnmt1-loxP*[2] brains, by shifting the balance from CXCL12/CXCR4
503 towards NRG3/ERBB4 signaling. Our data thus strongly suggests that DNMT1-mediated
504 repression of *Erbb4* promotes the migration of SST$^+$ cINs along the superficial migratory
505 stream. As Martinotti cells were described to migrate primarily along the MZ, while non-
506 Martinotti cells disperve via the SVZ[30], DNMT1 potentially contributes to the proper integration
507 of SST$^+$ cIN subtypes within the cortical migratory routes.
508
509 The migration of Martinotti cells along the MZ is functionally associated with the proper
510 formation of their axon collaterals in layer I[30]. These axon collaterals extend horizontally for up
511 to 2000 μm, making up approximately three-quarters (76%) of the GABAergic axons in this
512 layer[59]. This enables Martinotti cells to influence the activity of numerous pyramidal neurons,
513 which are their primary postsynaptic targets[59]. Hence, DNMT1 might also indirectly influence
514 the proper formation of these powerful axon collaterals in layer I, by promoting the migration
515 of SST$^+$ interneurons along the MZ. Lack of axon collaterals could contribute to the strong
516 functional and behavioral impairments that we observed for the adult *Sst-Cre/Dnmt1* KO mice,
517 despite the overall number not having been affected. This is in line with data from *Mafb* KO
518 mice, which also display a premature exit from the MZ and no changes in interneuron numbers
519 and distribution in adults. Yet, functional impairments were likewise observed[30].
520 Martinotti cells have densely branched axons within their originating layer and inhibit not only
521 pyramidal neurons but also other IN subtypes such as PV basket cells and vasoactive intestinal
522 peptide (VIP) bipolar cells. Together with the non-Martinotti cells, that are present across all
523 cortical layers, SST$^+$ cINs play crucial roles in modulating cortical circuitry, excitability, and
524 network synchronization[59]. It is therefore most likely that the altered SST$^+$ interneuron density,
525 evident in our mouse model due to shifts in cortical layer thicknesses, contributes to the
526 observed functional and behavioral deficits. However, *Dnmt1*-deletion may have also triggered
527 functional impairments in adult SST$^+$ interneurons. In PV interneurons, DNMT1 regulates
528 GABAergic transmission via DNA methylation-dependent transcriptional control of
529 endocytosis-related genes, which influences transmitter recycling[41]. *Dnmt1*-deletion in SST$^+$
530 interneurons could thus similarly result in disrupted synaptic signaling in these cells.
531
532 The *Dnmt1* deletion-induced changes in SST$^+$ interneuron migration were accompanied by
533 increased production of deep-layer neurons and altered IPC numbers at embryonic stages,
534 manifesting in larger deep and reduced upper layers in the adult cortex. This strongly implies,
535 that invading cINs influence cortical progenitors and the timed generation of cortical neurons.
536 As evidenced by Sessa et al. (2010)[46], the development of cortical interneurons and excitatory
537 neurons must have been effectively integrated throughout evolution, since an increase in the
538 production of excitatory neurons also necessitates a rise in interneuron generation to maintain

539 the proper balance of excitation and inhibition. Likewise, invading cINs could influence the
540 cortical progenitor cells. Indeed, it was already shown that cINs modulate EOMES$^+$ IPCs´
541 proliferation, and through this, act on the timed generation of cortical excitatory neurons[47]. This
542 aligns in part with our findings presented here, whereas the pair cell assay rather points to an
543 influence of cortical interneurons on RGCs through ephrinB2 - EPHA4 signaling, influencing
544 the generation of IPCs and neurons from these cells. External regulation of EPHA4-expressing
545 RGCs was already described for invading thalamic afferents, that import ephrinA5, another
546 ephrin ligand[5]. This signaling regulates the temporal balance of proliferative and neurogenic
547 divisions of apical progenitors. Both *efnA5* and *EphA4* deficiency cause an increased
548 production of deep-layer neurons due to a developmental change in the RGCs' neurogenic
549 potential[5].
550 Similarly, invading cINs are likely to import “external information” in the form of membrane-
551 bound or secreted signaling molecules, as we propose here. *Dnmt1* deletion in SST$^+$
552 interneurons caused increased *efnb2* expression, which is a ligand known to modulate cortical
553 neurogenesis. While progenitor-restricted *efnb2* deletion results in a delay in neurogenesis,
554 boosted ephrinB2 triggered EPHB signaling leads to a transient increase in neurons[48]. Similar
555 to our observations, the changes in neurogenesis measured by TBR1-positive cells were
556 restricted to a specific temporal window in the *efnB2* knockout mice, which aligns with our
557 results. This increase in neuronal production from RGCs was resembled in vitro with the pair
558 cell assay, stimulating RGC clones with ephrinB2-Fc. That changes in neuronal production at
559 specific embryonic stages can lead to altered layer thicknesses was already shown by other
560 studies[5,75].
561 In sum, the altered expression of secreted and membrane-bound signaling molecules with
562 known potential to regulate cortical progenitor division and fate, in concert with the altered
563 migration pattern of *Dnmt1* deficient SST$^+$ interneurons could lead to the altered cortical layer
564 formation. This suggests a crucial role for cortical interneurons in modulating the temporal
565 production of distinct subtypes of excitatory cortical neurons, and a high level of crosstalk
566 between immature cortical interneuron precursors and cortical progenitors to optimize the
567 formation of neural circuits. These findings also establish a key role for DNMT1 in orchestrating
568 cortical development through cell autonomous and non-cell autonomous actions.
569
570
571 **Acknowledgements**
572 This work was supported by the Flow Cytometry Facility and the Sequencing Facility, two core
573 facilities of the Interdisciplinary Center for Clinical Research (IZKF) Aachen within the Faculty
574 of Medicine at RWTH Aachen University. We thank Dr. Mira Jakovcevski and Ananya
575 Sangeetha for her experimental support, and Sandra Brill for her support with mouse care and
576 genotyping.
577
578
579 ***Author contributions***
580 J.R. performed experiments and data analysis, figure illustration, manuscript editing; P.W.
581 performed experiments and data analysis, figure illustration; J.D. performed experiments and
582 data analysis; C.L.F. performed experiments and data analysis; L.D. performed experiments
583 and data analysis; C.B.Y. performed experiments and data analysis; J.L. performed

experiments and data analysis; J.V. performed experiments and data analysis; S.K. performed experiments and data analysis; S.G. performed experiments and data analysis; G.N. methods support and data analysis; M.S. performed experiments and data analysis, C.C.K. data analysis; K.N.M. Data analysis, data discussion; T.V. data discussion and analysis; S.M. data analysis and discussion; G.Z.B. conceptual design, wrote the manuscript, data discussion.

Funding

This research was funded by the Deutsche Forschungsgemeinschaft (DFG, German Research Foundation)—368482240/GRK2416, ZI-1224/13-1.

Data Availability

The sequencing datasets generated and/or analyzed for this study are available in the Gene Expression Omnibus repository with the following accession numbers: GSE276510, GSE276512, and GSE276516. High-quality versions of all figures including those from the extended data are available under https://doi.org/10.6084/m9.figshare.26963338.

Figure Legends

Figure 1 – DNMT1 regulates hub genes of cIN development in E14.5 SST$^+$ interneurons

Differential gene expression and methylation analysis of *Sst-Cre/tdTomato* control (ctrl) and *Sst-Cre/tdTomato/Dnmt1 loxP*^{2} (*knockout;* KO) mice based on total RNA and enzymatic methyl-sequencing of FAC-sorted *tdTomato*$^+$ cells isolated from the E14.5 basal telencephalon. For RNA- and methyl-sequencing, we separately processed two samples per genotype, each consisting of cells pooled from multiple embryos (RNA sequencing: Ctrl $n = 23$ embryos; KO $n = 14$ embryos; methyl-sequencing: Ctrl $n = 15$ embryos; KO n = 11 embryos). **(a)** Heatmap depicting the 50 genes with the lowest adjusted *p*-values, color-coded based on relative expression. **(b)** Volcano plot depicting the differentially expressed genes (DEGs) between control and KO samples. Genes annotated as significantly changed (adjusted *p*-value < 0.05) are colored based on the fold change of the expression in the KO group. (**c**) Volcano plot of differentially methylated sites (DMS) identified in KO cells compared to control samples ($p < 0.001$ for color-labeled genes). **(d)** Venn diagram illustrating the overlap between up- or downregulated genes and genes associated with or containing a differentially methylated region (DMR). The intersection of upregulated and differentially methylated genes after knockout was tested for enrichment of the DNMT1 binding motif identified by DNMT1-ChIP-sequencing, shown in g. **(e)** DEGs identified in *Dnmt1* KO samples were compared to DEGs determined in embryonic stem cell-derived murine neurons overexpressing DNMT1 **(f)** Selection of brain development-related gene ontology (GO) terms enriched in genes that were both upregulated and differentially methylated in E14.5 *Sst-Cre/tdTomato/Dnmt1* KO cells. **(g)** DNA motif enriched in DNMT1-interacting chromatin, detected by ChIP-sequencing ($N = 2$ biological replicates). (**h**) Scatter plot combining DNA methylation changes and differential gene expression highlighting *Arx* as a potential target of DNA methylation-dependent transcriptional control by DNMT1. Bismark Methylation calls were filtered for a minimum of 3 reads per CpG and averaged for the promoter of each gene that was associated with a DMR and was either up or downregulated. Promoter regions were defined as 1kb upstream of the

629 TSS plus 100 bp into the gene body. **(i)** Position of differentially methylated regions relative to
630 the transcription start sites of genes related to cIN development. Horizontal bars indicate the
631 region's size, and color-coded is the mean methylation change for the respective region. **(j)**
632 RNA sequencing tracks combined with the methylation profile of the *Arx* gene locus obtained
633 from ctrl and KO samples.
634
635
636 **Figure 2: DNMT1 regulates the migration of SST⁺ interneurons in the developing cortex**
637 **at E14.5. (a)** Schematic illustration of a coronally sectioned E14.5 brain hemisphere, depicting
638 the migration routes of cortical interneurons. **(b, c)** Exemplary microphotographs of tdTomato-
639 positive interneurons in coronally sectioned (50 μm) hemispheres of *Som-Cre/tdTomato*
640 (control) **(b)** and of *Som-Cre/tdTomato/Dnmt1 loxP*^{2} (KO) embryos **(c)**. Scale bars: 500 μm.
641 **(d)** Quantitative analysis of the proportional distribution of tdTomato-positive cells in the basal
642 telencephalon and the cerebral cortex in E14.5 coronal sections (two-tailed nested *t*-test, n =
643 12 sections for control and n = 8 sections for KO, N = 3 embryos per genotype). **(e)**
644 Quantification of tdTomato-positive interneuron number within the cortex of control and KO
645 embryos normalized to the area, analyzed in 50 μm coronal cryosections (two-tailed nested *t*-
646 test n = 14 sections for control and n = 8 sections for KO, N = 3 embryos per genotype). **(f, g)**
647 Magnified microphotographs of the cortices of control and KO embryos (E14.5) to illustrate the
648 distribution of tdTomato⁺ cells within the cortical zones (MZ: marginal zone, CP: cortical plate,
649 IZ-VZ: intermediate zone to ventricular zone). White asterisks point to cells migrating along the
650 MZ (superficial migratory stream) or deep stream. Yellow arrows indicate tdTomato⁺
651 interneurons located in the CP. Scale bars: 100 μm. **(h)** Quantitative analysis of the
652 proportional distribution of tdTomato⁺ cells within the cortical zones normalized to the overall
653 tdTomato⁺-cell count within the cortex of control and KO embryos, analyzed in 50 μm coronal
654 cryosections (two-tailed nested *t*-test, n = 13 sections for control and n = 14 sections for KO,
655 N = 3 embryos per genotype). **(i, j)** Temporal z-projections of migration tracks of tdTomato-
656 positive cells in organotypic brain slice cultures (350 μm thickness, coronal) from E14.5 *Som-*
657 *Cre/tdTomato* (control) and *Som-Cre/tdTomato/Dnmt1 loxP*^{2} (KO) embryos, captured over
658 20 h by live-cell imaging. Scale bars: 500 μm. **k-n)** Quantification of the live-cell recordings in
659 organotypic brain slices. Quantitative analysis of the increase in fluorescence intensity in the
660 cortical plate due to invasion of tdTomato cells (first 12 h, two-tailed nested *t*-test, n = 4 slices
661 for control and n = 6 slices for KO embryos, N = 3 embryos per genotype) is shown in **(k)**, the
662 average number of directional changes (n = 134 cells across 5 slices for control (N = 4
663 embryos), n = 74 cells across 3 slices for KO (N = 3 embryos), two-tailed nested *t*-test) is
664 depicted in **(l)**. The velocity of all cells migrating within the cortex (n = 377 cells across 6 slices
665 for control (N = 5 embryos), n = 323 cells across 5 slices for KO (N = 3 embryos)) is shown in
666 **(m),** while the speed of cells within the area between CP and VZ is illustrated in **(n)** for control
667 (n = 193 cells across 6 slices, N = 5 embryos) and KO (n = 114 cells across 3 slices, N = 3
668 embryos); two-tailed nested *t*-test. **(o, p)** Selected frames extracted from live-cell imaging
669 recordings of organotypic brain slices (350 μm) derived from E14.5 control and KO embryos.
670 Depicted are tdTomato-positive cells migrating through the cortex. For each genotype, three
671 selected cells (dotted circles) were tracked. Scale bars: 50 μm.

672 Error bars represent the standard error of the mean (SEM). $p < 0.05$ *, $p < 0.01$ **, $p < 0.001$ ***;
673 n.s.: not significant. CP: cortical plate, VZ: ventricular zone, SVZ: subventricular zone, MZ:
674 marginal zone, IZ: intermediate zone.
675
676 **Figure 3: The *Dnmt1* deletion-induced effect on SST⁺ interneuron migration is**
677 **temporarily restricted. (a)** Exemplary microphotographs of tdTomato⁺ interneurons in
678 coronally sectioned (50 μm) hemispheres of E16.5 *Som-Cre/tdTomato* (control) and of *Som-*
679 *Cre/tdTomato/Dnmt1 loxP²* (KO) embryos; scale bars: 500 μm. TdTomato-positive cells are
680 labeled in red and DAPI in blue. Quantitative analysis of the proportional distribution of
681 tdTomato cells in the basal telencephalon and the cerebral cortex in E16.5 coronal sections
682 (two-tailed nested *t*-test, $n = 11$ sections for control and $n = 15$ sections for KO, $N = 4$ embryos
683 per genotype; error bars represent the standard error of the mean (SEM). **(c, d)** Magnified
684 microphotographs of the cortices of control and KO embryos from E16.5 coronal brain sections
685 (50 μm) to illustrate the distribution of tdTomato cells within the cortical zones. Scale bars: 100
686 μm. **(e)** Quantitative analysis of the proportional distribution of tdTomato cells within the E16.5
687 cortical zones normalized to the overall tdTomato-cell count within the cortex of control and
688 KO embryos, analyzed in 50 μm coronal cryosections. Two-tailed nested *t*-test, $n = 13$ sections
689 for control and $n = 14$ sections for KO, $N = 4$ embryos per genotype. **(f)** Quantitative analysis
690 of tdTomato cell density normalized to the given area of the respective cortical zones (E16.5,
691 two-tailed nested *t*-test, $n = 13$ sections for control and $n = 14$ sections for KO, $N = 4$ embryos
692 per genotype). **(g, h)** Exemplary microphotographs of tdTomato-positive interneurons in the
693 cortex of coronally sectioned (50 μm) brains of E18.5 *Som-Cre/tdTomato* (control) and *Som-*
694 *Cre/tdTomato/Dnmt1 loxP²* (KO) embryos; scale bars: 100 μm. **(i)** Quantitative analysis of the
695 proportional distribution of tdTomato cells within the E18.5 cortical zones normalized to the
696 overall tdTomato-cell count within the cortex of control and KO embryos, analyzed in 50 μm
697 coronal cryosections. Two-tailed nested *t*-test, $n = 11$ sections for control and $n = 9$ sections
698 for KO, $N = 4$ embryos per genotype, error bars represent the SEM. **(j)** Quantitative analysis
699 of tdTomato cell density normalized to the given area of the respective cortical zones (E18.5,
700 two-tailed nested *t*-test, $n = 11$ sections for control and $n = 9$ sections for KO, $N = 4$ embryos
701 per genotype). MZ: marginal zone, CP: cortical plate, IZ-VZ: intermediate zone to ventricular
702 zone. $p < 0.05$ *, $p < 0.01$ **, $p < 0.001$ ***, n.s.: not significant.
703
704
705 **Figure 4: Conditional deletion of *Dnmt1* in SST interneurons affects IPCs and the**
706 **generation of TBR1⁺ cells non-cell autonomously. (a)** Schematic illustration of a coronally
707 sectioned embryonic brain hemisphere, depicting the lateral and dorsal localization of the two
708 bin selections, used to quantify the density and distribution of EOMES⁺- and TBR1⁺-cells in
709 E14.5 and E16.5 brain sections. **(b-e)** TBR1 and EOMES immunostaining in coronally
710 sectioned (50 μm) brains of E14.5 *Sst-Cre/tdTomato* (control) and *Sst-Cre/tdTomato/Dnmt1*
711 *loxP²* (KO) embryos. **(b** and **d)** Exemplary microphotographs of (**b**) TBR1 immunostaining
712 (green) and **(d)** EOMES immunostaining (green); scale bars: 50 μm (DAPI is shown in blue).
713 **(c** and **e)** Quantitative analysis of the TBR1⁺ postmitotic neuron numbers **(c)** and EOMES⁺
714 intermediate progenitor cell (IPC) numbers **(e)** per bin in the E14.5 cortex of control and KO
715 embryos, analyzed in 50 μm coronal cryosections (two-way ANOVA with subsequent

716 Bonferroni correction, n = 13 control and n = 9 KO sections from N = 3 embryos for both
717 genotypes). **(f)** TBR1 immunostaining (green) in coronally sectioned (50 μm) brains of E16.5
718 control and KO embryos, scale bars: 50 μm. **(g)** Quantitative analysis of the TBR1-positive
719 postmitotic neuron numbers per bin in the E16.5 cortex of control and KO embryos, analyzed
720 in 50 μm coronal cryosections (two-way ANOVA with subsequent Bonferroni correction, n = 8
721 for control and KO from N = 3 embryos for both genotypes). **(h** and **j)** Exemplary
722 microphotographs of (**h**) EOMES immunostaining (green) and **(j)** TBR1 immunostaining
723 (green) in coronal sections of E18.5 control and KO brains; scale bars: 50 μm (DAPI is shown
724 in blue). **(i** and **k)** Quantitative analysis of the density of EOMES-positive IPCs **(i)** and TBR1-
725 positive postmitotic neurons **(k)** in the E18.5 cortex of control and KO embryos, analyzed in 50
726 μm coronal cryosections (two-tailed nested *t*-test, n = 11 sections for both genotypes from N =
727 4 embryos per genotype). **(l)** Schematic illustration of the cortex of a coronally sectioned
728 embryonic brain (E18.5), depicting the parameters analyzed for the quantification shown in
729 (**m**). Three regions (lateral (1), dorsolateral (2), and dorsal (3)) were averaged to obtain the
730 mean thickness respectively for each layer (two tailed nested *t*-test; n = 12 control and n = 9
731 KO sections. N = 4 brains for both genotypes). **(n** and **o)** Panels depict significant ligand-
732 receptor pairs involved in communication from SST$^+$ cINs to cortical progenitors, filtered by
733 differentially expressed genes (DEG) from single-cell RNA-sequencing data. Communication
734 probability is represented by dot color, and *p*-value by dot size, with *p*-values being computed
735 using a one-sided permutation test. Panel (**n**) shows the communication with different apical
736 progenitor (AP) populations at E14.5. Panel **(o)** illustrates communication with IPCs at E14.5.
737 Panels **(p andr)** present microphotographs of cell pair combinations formed from cortical
738 neurons isolated from E14.5 C57BL6/J embryos, plated at clonal density, after 24 hours. Cell
739 clones were either treated with control (ctrl.)- or recombinant efnB2-FC for 24 h, before
740 immunocytochemical staining for Nestin (magenta), β-III-tubulin (TUBB3, green), EOMES
741 (TBR2, yellow) and DAPI (blue). Scale bars: 5 μm. **(q and s)** Quantification of the proportion
742 of Nestin/Nestin (2xN), β-III-tubulin/β-III-tubulin (2xT), Nestin/β-III-tubulin (N-T), EOMES-
743 EOMES (2xE), and Nestin-EOMES (N-E) positive cell pairs normalized to the overall number
744 of these pairs. Unpaired, two-tailed Student's *t*-test with subsequent Welsh's correction (panel
745 q: control-Fc: 66 cell pairs, efnB2-Fc: 58 cell pairs, from N = 3 experiments; panel s: control-
746 Fc: 71 cell pairs, efnB2-Fc: 73 cell pairs, from N = 4 experiments). $p < 0.05$ *, $p < 0.01$ **, $p <$
747 0.001 ***. MZ: marginal zone, CP: cortical plate, IZ-VZ: intermediate zone-ventricular zone,
748 ctrl.: control, n.s.: not significant, ctrl: control.
749
750
751 **Figure 5: Adult *Dnmt1*-deficient mice show aberrant cortical architecture and**
752 **functionality. (a-d)** Immunostaining using an antibody directed against parvalbumin (PV) in
753 50 μm brain sections of six-month-old *Sst-Cre/tdTomato* (control) and *Sst-*
754 *Cre/tdTomato/Dnmt1 loxP*^{2} (KO) mice show increased proportions of PV$^+$ *Sst-Cre/tdTomato*
755 neurons upon *Dnmt1* deletion. Exemplary microphotographs of immunostainings (tdTomato in
756 red, PV in green, DAPI in blue) taken from the primary somatosensory cortex (S1) of coronal
757 slices (Bregma 0.14, -0.22, and -0.34) from (**a**) control and (**b**) KO mice. Scale bars: 100 μm
758 (left panels) and 20 μm (magnifications of marked selections). **(c)** Quantification of the
759 proportion of PV-positive *Sst-Cre/tdTomato* cells over the whole S1 as well as in supra- and
760 infragranular layers normalized to the total amount of all detected *Sst-Cre/tdTomato* cells. Two-

761 tailed nested *t*-test with $n = 11$ slices for control and $n = 10$ for KO from $N = 3$ brains for both
762 genotypes. **(d-g)** *Dnmt1* KO mice display changes in cortical layer thickness alongside
763 alterations in *Sst-Cre/tdTomato* cell density. **(d, e)** Exemplary microphotographs of
764 immunostainings of CUX1 and tdTomato combined with DAPI taken from S1 (sagittal slices of
765 Bregma 1.32 and 1.44, six-month-old male mice). The CUX1-positive upper layers II-IV can
766 be distinguished from deep layers V and VI. Scale bars: 100 μm. **(f, g)** Quantification of the
767 tdTomato-positive cell density normalized to the given area of the respective layers (**f**), the
768 cortical thickness, and the proportional thickness of the deep and upper layers (**g**). Two-tailed
769 nested *t*-test with $n = 24$ slices for control and $n = 23$ for KO from $N = 3$ brains for both
770 genotypes. **(h-q)** Neuropixels recordings in S1 of adult *Sst-Cre/tdTomato* (control) and *Sst-*
771 *Cre/tdTomato/Dnmt1 loxP*^{2} (KO) mice (n = 8 sessions from 2 mice per genotype), while animals
772 were receiving either tactile stimulation by air puffs against their whiskers or visual stimuli **(h)**.
773 **(i)** Average local field potential (LFP) in S1 across the whole cortical depth, following a 20 ms
774 air puff stimulus (onset at white line) to the distal whisker pad. Blue colors indicate negative,
775 and yellow colors positive LFP responses. Across all layers, LFP responses were stronger and
776 more temporally precise in control mice (left) compared to KO mice (right). **(j)** Average current
777 source density (CSD) in S1 calculated from the measured LFP. Blue colors indicate excitatory
778 and yellow colors inhibitory currents. The earliest responses in control mice (left) occur in the
779 granular layer at ~400 μm cortical depth and then spread to layer II/III (100-300 μm) and layer
780 V (500-900 μm). In contrast, no clear spatial response profile is visible in KO mice, suggesting
781 a disruption of cortical network function. **(k)** Traces of LFP responses in S1 depicting averaged
782 LFPs across all cortical layers (0 - 1 mm) for recordings in control (gray) and KO (orange) mice
783 (shading indicates the standard error of the mean (SEM)) illustrate significantly larger and
784 faster tactile responses in control mice compared to KO mice (peak amplitude$_{control}$ = -159.09
785 ± 34.37 µV, peak amplitude$_{KO}$ = -57.17 ± 7.49 µV; Wilcoxon *rank-sum* test, $p = 0.0059$; peak
786 time$_{control}$ = 26.85 ± 26.85 ms, peak time$_{KO}$ = 30.80 ± 1.10 ms, $p = 0.0108$). **(l-o)** Quantification
787 of the temporal precision of the spiking response of S1 neurons to tactile stimulation in control
788 (gray) and KO (orange) mice. **(l)** Peristimulus time histogram (PSTH) for spiking response of
789 S1 neurons to tactile stimulation in KO (orange) and control mice (gray). **(m)** The width of the
790 initial response, measured as the full width at half maximum (FWHM), was significantly larger
791 in KO compared to control mice (n = 298 clusters, Wilcoxon *rank-sum* test, $p = 7\text{x}10^{-31}$). **(n)**
792 Quantification of early tactile response amplitude in control versus KO mice. In the first 30 ms
793 after tactile stimulation, responses in control mice were significantly larger compared to KO
794 mice (mean firing rate$_{control}$ = 9.09 ± 0.31 Hz, $n = 436$ clusters, mean firing rate$_{KO}$ = 7.22 ± 0.32
795 Hz, $n = 298$ clusters, Wilcoxon rank-sum test, p = 0.000045). **(o)** Late tactile responses in KO
796 mice were significantly larger compared to control mice (mean firing rate$_{control}$ = 0.4 ± 0.10 Hz,
797 $n = 436$ clusters, mean firing rate$_{KO}$ = 3.85 ± 0.43 Hz, n = 298 clusters, Wilcoxon *ranksum*
798 test, $p = 4\text{x}10^{-37}$). **(p)** Absolute spectral power density (ASPD) of LFP recordings across all
799 layers in primary visual cortex (V1) during full-field visual stimulation in control (left) and KO
800 mice (right). Hot colors indicate higher spectral power, units are on a $\log_{-10}$ scale. Spectral
801 power falls off with frequency but shows increased activity in the higher frequency range >
802 20Hz between 0.3- and 0.7-mm cortical depth for control mice. In contrast, no clear modulation
803 of higher frequencies was found in KO mice. **(q)** Relative change in spectral power during
804 visual stimulation, computed as the percent difference relative to baseline. In control mice (left),
805 visual stimulation induced a strong increase in the gamma range (> 30Hz), especially at around

70 Hz between 0.3- and 0.7-mm cortical depth. In contrast, no clear modulation was found in KO mice (right). $p < 0.05$ *, $p < 0.01$ **, $p < 0.001$ ***, n.s.: not significant.

Figure 6: Adult *Dnmt1*-deficient mice show behavioral abnormalities. (a-e) Nest building test reveals a significant deterioration in using given material and forming proper nests in adult *Sst-Cre/tdTomato/Dnmt1* loxP[2] (KO) individuals compared to *Sst-Cre/tdTomato* (control) mice. With the help of the scoring index depicted in **(a)** and formerly described[73], all mice were ranked based on nest quality and amount of material used **(d, e)**. Representative photographs are shown in **(b)** for control and **(c)** for KO mice. Tests were performed overnight and twice within one week. Respective values were averaged for both trials. Unpaired, two-tailed Student's *t*-test with subsequent Welch's correction. N = 16 male adult mice for both genotypes. **(f-h)** Pentylenetetrazol (PTZ)-injections point to defects in cortical inhibition in KO mice. **(f)** Schematic illustration defining PTZ-induced seizures in three-month-old males, that received intraperitoneal injections of PTZ every ten minutes until displaying a final tonic-clonic seizure (event IV) within a time window of a maximum of 120 minutes. Footages captured from video monitoring of PTZ-induced convulsions defining criteria for small seizures (events I and II) and tonic-clonic seizures (III and IV). **(g, h)** Quantification of seizure profiles of control (N = 9) and KO individuals (N = 6). Unpaired, two-tailed Student's *t*-test with subsequent Welch's correction. $p < 0.05$ *, $p < 0.01$ **, $p < 0.001$ ***.

Methods:

Animals

In the recent study transgenic mouse strains with a genetic C57BL/6J background (initially obtained from the University Hospital UKA Aachen, Germany) were used. *Sst*$^{tm2.l(cre)Zjh}$/J x *B6.CgGt(ROSA)26Sor*$^{tml\ 4(\ CAG\text{-}tdTomato\ )Hze}$ (*Sst*$^{+/-}$*-Cre/tdTomato)* served as control animals whereas *Sst*$^{tm2.l(cre)Zjh}$*/J* x B6.CgGt(ROSA)26Sor$^{tm14(CAG\text{-}tdTomato)Hze}$ x *B6; 129S-Dnmt1tm4Jae*/J (*Sst-Cre*$^{+/-}$*/tdTomato/Dnmt1 loxP*^{2}*)* were used as *Dnmt1* knockout (KO) model.

Generation of control animals was conducted by crossing a *Sst*$^{tm2.l(cre)Zjh}$/J strain (RRID:IMSR_JAX:013044, Jackson Laboratory, Bar Harbour, U.S.A.) with a t*dTomato* reporter mouse model (*B6.CgGt(ROSA)26Sor*$^{tml\ 4(\ CAG\text{-}tdTomato\ )Hze}$*,* obtained from Christian Hübner, University Hospital Jena, Germany). An *internal ribosomal entry site* (*IRES*), a *Cre-recombinase* sequence, a *polyA* sequence, and a *frt*-flanked neo cassette were inserted into the 3' untranslated region (UTR) of the *Somatostatin (Sst)* locus on chromosome 16, limiting the respective *Cre*-expression to *Sst*-positive cells. The t*dTomato* reporter strain was characterized by the corresponding *tdTomato* sequence combined with a *loxP*-flanked stop cassette, both located in the *Rosa26* locus. Expression of *Cre-recombinase* dependent on *Sst*-promoter activity resulted in the deletion of the *loxP*-flanked stop cassette during recombination and a final expression of *tdTomato* in *Sst-Cre*-positive cells. *Jackson Laboratory* recommends creating and breeding *Sst-Cre* heterozygous mice[77], which received the *Cre*-allele from the

850 maternal side. This strategy avoids potential instability of the Cre-recombinase activity during
851 paternal germline recombination[77].
852 To generate the triple transgenic conditional KO-model *Sst-Cre*$^{+/-}$*/tdTomato* females were bred
853 with male individuals derived from crossing *tdTomato* mice with a *Dnmt1 loxP*^{2} strain (*B6;*
854 *129Sv-Dnmt1tm4Jae/J,* obtained from Rudolf Jaenisch, Whitehead Institute for Biomedical
855 Research Boston, U.S.A.) in which exon 4 and 5 of the *Dnmt1* gene are loxP-flanked, resulting
856 in a null allele of these loci and a subsequent DNMT1 deficiency[78]. Corresponding programs
857 and primers used for genotyping can be found in the supplementary information. An illustration
858 of control- and KO mice is shown in Extended Data Figure E1a.
859
860

861 **Isolation of Embryonic and Adult Brains**

862 Individuals of embryonic stage 14.5, 16.5 or 18.5 were isolated as described in Symmank et
863 al. (2018)[79]. Briefly, pregnant females were anesthetized by intraperitoneal administration of
864 ketamine/xylazine (200/25 mg/kg living weight per injection up to a maximum application of
865 600/75 mg ketamine/xylazine per kg living weight in total). Upon reaching surgical tolerance,
866 the abdominal cavity was opened to expose the uterine horns that were removed. Embryos
867 were isolated from the uteri and decapitated. For histological analyses of E14.5 and E16.5
868 brains, the heads were directly transferred to 4% paraformaldehyde (PFA)/1x phosphate-
869 buffered saline (PBS). For histological analyses at E18.5, brains were removed from the skull
870 before transferring them to 4% PFA/1x PBS. E14.5 heads were fixed for 5 hours, while E16.5
871 heads and E18.5 brains were fixed overnight at 4 °C on an orbital shaker (50 rpm). Afterwards,
872 stepwise cryopreservation was performed by overnight incubation first in 10% Sucrose/1x
873 PBS, followed by 30% sucrose/1x PBS at 4 °C on an orbital shaker (50 rpm). Tissue was
874 frozen in liquid nitrogen and stored at -80 °C.
875
876 For the isolation of adult brains, male mice were sacrificed with an overdose of 5% (v/v)
877 isoflurane. For histological analyses and identification of Neuropixels recording sites,
878 transcardial perfusion was conducted with 1x PBS (pH 7.4) followed by 4% PFA/1x PBS
879 (pH 7.4) with a pump[80]. After brain preparation, post-fixation was conducted in 4% PFA/1x
880 PBS for 24 h at 4°C on a roller mixer with constant rotation (approx. 50 rpm). Then,
881 cryopreservation was performed in 10% sucrose/1x PBS and 30% sucrose/1x PBS for 24 h
882 each at 4°C on a roller mixer with constant rotation (approx. 50 rpm) before brains were frozen
883 in liquid nitrogen and stored at -80°C.
884

885 **Organotypic brain slices and single-cell preparations**

886 MGE- and cortical single cells were prepared as described previously[19,41]. Briefly, embryonic
887 heads were collected and dissected in Gey's Balanced Salt Solution (GBSS, pH 7.4)/0.65%
888 D-glucose on ice. MGEs and cortices were cut out and collected in Hanks' Balanced Salt
889 Solution (HBSS, w/ phenol red, w/o calcium, w/o magnesium)/0.65% D-glucose on ice. The
890 tissue was treated with 0.04% of trypsin/EDTA (Thermo Fisher Scientific, U.S.A.) for 17 min at
891 37°C, before MGE cells were dissociated in cold Dulbecco's Modified Eagle Medium (DMEM)
892 with additional L-glutamine and 4.5 g/L D-glucose (Thermo Fisher Scientific, U.S.A.), 10% fetal
893 bovine serum (FBS; Biowest, U.S.A.), and 1% penicillin/streptomycin (P/S) (Thermo Fisher

894 Scientific, U.S.A.) by trituration with glass Pasteur pipettes and by subsequent filtering through
895 a nylon gauze (pore size 140 μm; Merck, U.S.A.). Dissociated single cells were seeded on
896 laminin (19 μg/ml; Sigma-Aldrich, U.S.A.)/poly-L-lysine- (10 μg/ml; Sigma-Aldrich, U.S.A.)
897 coated glass coverslips. For MGE cells, we used a density of 455 cells/mm^2. Cortical single
898 cells were seeded in clonal densities of 150 cells/mm^2. Transfection of MGE cells with siRNA
899 oligos occurred after 5–6 h of incubation (37°C, 5% CO_2 and 95% relative humidity) in
900 Neurobasal medium with phenol red, 1x B27™, and 0.25x GlutaMAX (Gibco, U.S.A.) for 24 h.
901 For this, the medium was supplemented with Lipofectamine™ 3000 in accordance with the
902 manufacturer's instructions (Thermo Fisher, U.S.A.) together with *Dnmt1* siRNA (30 nM, #sc-
903 35203, Santa Cruz, U.S.A.) and a scrambled control siRNA construct (15 nM, BLOCK-iT™
904 Fluorescent Oligo, #2013, Thermo Fisher, U.S.A.). After 24 h MGE cells were fixated with 4%
905 PFA/1x PBS for 10 min.
906 Incubation of cortical cells plated at clonal density occurred at 37°C, 5% CO_2 and 95% relative
907 humidity in culture medium (Neurobasal medium with phenol red, 1x B27™, 0.25x GlutaMAX
908 (Gibco, U.S.A.), and 0.4% methylcellulose (Sigma, U.S.A.)) for 24 h. Treatment of cortical
909 single cells was conducted 5–6 h after plating. For this, the medium was supplemented with
910 10 μM 5-ethynyl-2′-deoxyuridine (5-EdU, baseclick™, baseclick GmbH, Germany) and with
911 either 5 μg/mL of a recombinant human Fc control protein (Rockland Immunochemicals,
912 U.S.A.) or 5 μg/mL of a recombinant human efnB2-Fc (R&D Systems, U.S.A.). Both
913 recombinant proteins were pre-clustered with 10 μg/mL of an anti-human IgG antibody
914 (Thermo Fisher, U.S.A.). Cortical single cells were fixated with 4% PFA/1x PBS for 10 min.
915 For organotypic brain slice preparations[27], brains of E14.5 embryos were embedded in 4% low
916 melt agarose (37°C) in Krebs buffer (126 mM NaCl, 2.5 mM KCl, 1.2 mM NaH_2PO_4, 1.2 mM
917 $MgCl_2$ * $6H_2O$, 2.1 mM $CaCl_2$; pH 7.4; supplemented with 10 mM D-glucose and 12.5 mM
918 $NaHCO_3$, sterile-filtered). For sectioning of 350 μM coronal slices, a 5100mz-Plus vibrating
919 microtome (speed: 0.7–0.8 mm/s and blade oscillation frequency: 5 Hz; Camden Instruments,
920 United Kingdom) was used. Slices were transferred to ice-cold post-holding buffer (1x Krebs
921 buffer, 10 mM HEPES, 1% P/S, 0.2% gentamycin, pH 7.4). Slices were imaged in μ-slide 4
922 Well imaging plates (ibidi GmbH, Germany) coated with 19 μg/mL laminin (Sigma-Aldrich,
923 U.S.A.) and 10 μg/mL poly-L-lysine (Sigma-Aldrich, U.S.A.) in Neurobasal without phenol red,
924 1x B27™, 1% P/S, 0.5% D-glucose, 10 mM HEPES, using a confocal-like Leica DMi8
925 fluorescent microscope in combination with a THUNDER® imager unit (Leica, Germany) and
926 the corresponding software *LASX* (Leica, Germany) equipped with an incubation chamber
927 (37°C, 5% CO_2 and 95% relative humidity). Imaging was conducted with a wavelength of
928 544 nm (TRITC-channel) in tile scans including z-stacks of 8–10 μm step size every 15 min.
929 Post-processing of the respective footages was executed in the *LASX* software using the
930 "*Mosaic Merge*"- and "*Thunder Lightning (Large Volume)*"-tools. Finally, a maximum intensity
931 projection of the merged tile scans was processed using the *Fiji* software[81]. Analysis was
932 performed blindly using the manual track plugin from ImageJ (NIH, USA) to track cells with a
933 migration time of at least 6 h.
934
935 **Histology and immunocytochemistry**
936 For histology on embryonic brains, we used 50-μm coronal brain slices, cryosectioned with a
937 CM3050 S Cryostate (Leica, Germany), and collected on Superfrost®Plus (Avantor, U.S.A.)
938 object slides. On-slide immunohistochemistry was performed as described in Pensold et al.

(2017)[27]. Briefly, all samples were washed for 5x 20 min in 1x PBS /0.5% Triton X-100/0.5% Tween®20 with constant horizontal shaking (50 rpm). After that all samples were treated with blocking solution (4% bovine serum albumin (BSA) and 10% normal goat serum in 1x PBS/0.5% Triton X-100/0.5% Tween®20) was applied for 2 h at room temperature (RT). Primary antibody incubation diluted in blocking solution was conducted overnight at RT in a humid chamber. After washing for 5x 20 min in 1x PBS/0.5% Triton X-100/0.5% Tween®20, secondary antibodies were applied in blocking solution for 2h at RT. After washing for 3 x 20 min, the samples were stained with 4',6-diamidino-2-phenylindol dihydrochloride (DAPI, 1:10000 in PBS, Carl Roth, Germany) for 15 min at RT, followed by washing twice for 5 min with PBS, sections were embedded in Mowiol.

For adult brains, immunohistochemistry was performed in free-floating sagittal and coronal sections (30 μm), prepared using the CM3050 S Cryostate (Leica, Germany). Slices were transferred to 1x PBS and stored at 4°C. For sagittal sections, Bregma 1.32 and 1.44 were used, while Bregma 1.18, 1.10, 0.14, -0.22, -3.08, and -3.28 were taken for coronal sections. The same procedure as for embryonic sections was applied, except that an antigen retrieval with heated HistoVT One® (1x HistoVT One®/H_2O bidest., Nacalai, Japan) at 70°C for 20 min was performed for staining against DNMT1. Sections that were stained for somatostatin, calretinin, and NPY underwent an antigen retrieval with citrate buffer (95°C; 10 mM, pH 6.0, supplemented with 0.5% Tween®20) for 15 min and subsequent cool-down for 30 min before washing. Finally, all slices were transferred onto glass slides in 0.5% (w/v) gelatine/0.05% (w/v) chromium(III) potassium sulfate dodecahydrate ($KCrS_2O_8$)/H_2O solution prior to embedding in Mowiol.

Immunostaining on dissociated MGE and cortical single cells was conducted by washing coverslips with 1x PBS/0.1% Triton X-100 for 3x 5 min and blocking with 1x PBS/0.1% Triton X-100/4% BSA for 30 min at room temperature. Primary antibodies were applied for 2 h at room temperature. After washing for 3x 5 min with 1x PBS/0.1% Triton X-100, the secondary antibody was incubated for 1 h at room temperature. Phalloidin-647 diluted 1:1000 in 1x PBS (#ab176759, Abcam, U.S.A.) was applied for 20 min after washing. Then a final washing step with 1x PBS for 10 min and a DAPI staining (1:10000/1x PBS; Carl Roth, Germany) for 5 min were performed and coverslips were mounted in Mowiol.

The applied primary antibodies were used: mouse anti-Calretinin (1:500; Swant, Switzerland, #6B3), rabbit anti-NPY (1:2500; Immunostar, U.S.A., #2940), rabbit anti-TBR1 (1:200; Abcam, U.S.A., #ab31940); rabbit anti-EOMES (1:500; Abcam, U.S.A., #ab23345); rat anti-Somatostatin (1:100; Millipore, U.S.A., #MAB354), mouse anti-Parvalbumin (1:2000; Swant, Switzerland, #235); rabbit anti-DNMT1 (1:100; Santa Cruz, U.S.A., # sc20701); rabbit anti-CUX1 (CDP; 1:100, Santa Cruz, U.S.A., #sc13024); mouse anti-Nestin (1:100; Merck U.S.A., #MAB353), rabbit anti-ß-Tubulin III (1:500; Sigma Aldrich, U.S.A., #T2200), and rabbit anti-ErB4 (1:1000; Proteintech, U.S.A., #22387-1-AP).

The following secondary antibodies conjugated with respective fluorophores were used at 1:1000 dilutions: Alexa488-goat anti-Rat IgG (Invitrogen, U.S.A., #A11006) Cy5-Goat anti-Rabbit IgG (Life Technologies, U.S.A., #A10523), A488-Donkey anti-Mouse IgG (Jackson, U.S.A., #15454150), Cy5-Goat anti-Mouse IgG (Jackson, U.S.A., #115175146), A488-Goat anti-Rabbit IgG (Life Technologies, U.S.A., #A11008).

983 **Transcriptome data on neurons overexpressing DNMT1**
984 *Dnmt1$^{tet/tet}$* mouse embryonic stem cells have been previously described[82]. The levels of
985 DNMT1 in these cells are four times higher than the normal wild-type *R1* ESCs. Upon
986 differentiation, the induced *Dnmt1$^{tet/tet}$* neurons produced contain twice the DNMT1 levels than
987 in *R1* neurons[82]. Differential expression gene data on *Tet/Tet* neurons was taken from Singh
988 *et al*. (2023)[83] and genes with significantly altered transcript levels were compared with the
989 transcriptome data on the tissues lacking DNMT1.
990
991 **Preparation of E14.5 tdTomato cells for RNA and methyl-sequencing**
992 For FACS-mediated enrichment of E14.5 *Sst-Cre/tdTomato* cells, the whole basal
993 telencephalon was prepared from the embryos and subjected to cell dissociation. Nuclease-
994 free reaction tubes were used during isolation and long-term storage of the resulting material.
995 The basal telencephalons were collected in cold HBSS (w/ phenol red, w/o calcium, w/o
996 magnesium)/0.65% D-glucose; 4 μg/μL (600 U) of DNAse I (AppliChem GmbH, Germany).
997 After treatment with 0.04% trypsin for 17 min at 37 °C, HBSS was replaced by DMEM with
998 additional L-glutamine and 4.5 g/L D-glucose, 10% FBS and 1% P/S to stop the trypsinization.
999 Subsequently, the cells were pelletized, resuspended and triturated in cold HBSS (w/o phenol
1000 red, w/o calcium, w/o magnesium)/0.65% D-glucose, before being filtered through a nylon
1001 gauze (pore size 140 μm, Merck, U.S.A.) for FACS.
1002 FACS was performed by the Flow Cytometry Facility (FCF, University Hospital RWTH Aachen,
1003 Germany). Respective parameters for the procedure using a BD FACS Aria Fusion (BD
1004 Biosciences, U.S.A) were defined as follows: 5-laser (FCS, SSC, PE, BV421), 18-color (3-6-
1005 2-4-3). TdTomato-positive cells were either collected in 100 μL of cold TRIzol™ (Thermo
1006 Fisher Scientific, U.S.A.) for subsequent RNA sequencing or in 100 μL of cold HBSS (w/o
1007 phenol red, w/o calcium, w/o magnesium)/0.65% D-glucose for further processing for DNA
1008 methylation analysis. Finally, all samples were stored at -80°C.
1009
1010 **Total RNA seq**
1011 TdTomato-positive E14.5 MGE cells from *Sst-Cre/tdTomato or Sst-Cre/tdTomato/ Dnmt1*
1012 *loxP*[2] were FAC sorted into 100 μL TRIzol™ reagent (Thermo Fisher Scientific, U.S.A.).
1013 Samples were mixed by inversion and stored at -80°C until processing. RNA was isolated from
1014 50,000 cells pooled per genotype. The samples were filled up to 1 ml with TRIzol™ and
1015 dounced 25 times in a glass homogenizer using the small-clearance pestle. Samples were
1016 incubated for 5 min at room temperature, supplemented with 200 μL chloroform, and mixed by
1017 shaking vigorously until a homogenous milky solution appeared. Following another incubation
1018 at room temperature (until a visible phase separation appeared) samples were centrifuged at
1019 13,000x *g* and 4°C for 15 min in a tabletop centrifuge with cooling function. For precipitation,
1020 the clear upper phase was collected and mixed with 70% ethanol. Samples were bound onto
1021 RNeasy mini columns (Qiagen, Germany) and washed according to the instructions in the
1022 manual. RNA was eluted with 30 μL nuclease-free water.
1023 RNA concentrations were determined using a Qubit™ 4 flourometer (Thermo Fisher Scientific,
1024 U.S.A.) with RNA HS reagents (Thermo Fisher Scientific, U.S.A.). RNA integrity was checked
1025 on a Tape Station 4200 using the HS RNA kit (Agilent Technologies, U.S.A.).
1026 Prior to library preparation, samples were digested with HL dsDNAseI (ArcticZymes
1027 Technologies ASA, Norway) for 10 min at 37°C to remove traces of gDNA. To avoid digestion

of the newly generated cDNA during library preparation, the dsDNAseI was heat-inactivated for 5 min at 58°C. Thereafter, samples were subjected to library preparation using the TAKARA SMARTer Stranded Total RNA-Seq Kit v3 - Pico Input Mammalian for Illumina (Takara Bio, Japan). Fragmentation was done at 94°C for 4 min. Illumina adaptors and indices were ligated to cDNA in a PCR reaction with 5 cycles (98°C for 15 s, 55°C for 15 s and 68°C for 30 s). RRNA depletion was performed on the amplified libraries. Final libraries were subjected to an upscale PCR with 13 cycles (98°C for 15 s, 55°C for 15 s and 68°C for 30 s). Amplified libraries were cleaned with magnetic AMPure XP beads (Beckman Coulter, U.S.A.). Library concentration was determined with a Qubit™ 4 fluorometer using the 1x dsDNA HS reagent (Thermo Fisher Scientific, U.S.A.). Library size was assessed on a Tape Station 4200 using the DNA D1000 kit (Agilent Technologies, U.S.A.).
Libraries were diluted, equimolarly pooled, denatured, and loaded for clustering onto an Illumina NovaSeq 6000 SP (200 cycles) flow cell (Illumina, U.S.A.) in conjunction with 1% PhiX control library, and run on an Illumina NovaSeq machine (Illumina, U.S.A.) in 75 bp paired-end mode. The 1% PhiX control library was spiked in to improve base calling accuracy.

FASTQ files were generated using *bcl2fastq* (Illumina, U.S.A.). To facilitate reproducible analysis, samples were processed using the publicly available *nf-core/rnaseq* pipeline version 3.12[84] implemented in Nextflow 23.10.0[85] with minimal command. In brief, lane-level reads were trimmed using *Trim Galore* 0.6.7[86] and aligned to the mouse genome (GRCm39) using *STAR 2.7.9a*[87]. Gene-level and transcript-level quantification was done by *Salmon v1.10.1*[88]. All analysis was performed using custom scripts in *R versio*n 4.3.2 using the *DESeq2 v.1.32.0* framework[89].

MethylSeq

TdTomato-positive E14.5 MGE cells from *Sst-Cre/tdTomato* and *Sst-Cre/tdTomato/ Dnmt1 loxP*[2] were FAC-sorted into 100 µL HBSS. Samples were mixed by inversion and stored at -80°C until processing.
DNA was isolated from at least 50.000 pooled cells per sample using the PureLink genomic DNA Mini Kit (Thermo Fisher Scientic, U.S.A.). Per genotype, the samples were initially pooled by volume (200 uL each), supplemented with lysis buffer provided in the kit and incubated with 2 µL proteinase K (Thermo Fisher Scientific, U.S.A.) at 55°C for 10 min. DNA was precipitated with 100% ethanol. Samples were bound to one column per genotype each, washed as instructed, briefly dried and eluted with 35 µL Tris-EDTA (TE) buffer. DNA concentrations were determined using the Qubit™ 4 flourometer with the 1x dsDNA HS reagent (Thermo Fisher Scientic, U.S.A.). Quality/integrity was checked on a Tape Station 4200 using the Genomic DNA kit (Agilent Technologies, U.S.A.).
Libraries were generated using the Enzymatic Methyl-seq kit for Illumina (#E7120, New England Biolabs, U.S.A.). After enzymatic shearing for 25 min at 37°C with the NEBNext UltraShear enzyme and buffer, followed by an inactivation at 65°C for 15 min, 5-methylcytosines were oxidized by TET2 after adaptor ligation. Samples were denatured with formamide and deaminated with APOBEC. Libraries were subjected to 7 cycles of upscale PCR (98°C for 10 s, 62°C for 30 s, and 65°C for 60 s). Library concentrations were determined with a Qubit™ 4 fluorometer and the 1x dsDNA HS reagent (Thermo Fisher Scientific, U.S.A.).

1073 All recommended clean-up steps were performed with magnetic AMPure XP beads (Beckman
1074 Coulter, U.S.A.). Library size was assessed on a Tape Station 4200 using the DNA D5000 kit
1075 (Agilent Technologies, U.S.A.). Concentrations were determined with a Qubit™ 4 fluorometer
1076 and the 1x dsDNA HS reagent (Thermo Fisher Scientific, U.S.A.).
1077 Libraries were diluted, equimolarly pooled, denatured, and clustered onto an Illumina NextSeq
1078 500/550 Mid Output Kit v2.5 (300 cycles) flow cell (Illumina, U.S.A.). The 1% PhiX control
1079 library was spiked in to improve base calling accuracy. Paired-end sequencing was performed
1080 with 151 cycles.
1081 FASTQ files were generated using bcl2fastq (Illumina, U.S.A.). To facilitate reproducible
1082 analysis, samples were processed using the publicly available nf-core/methylseq pipeline
1083 version 2.6.0[84] implemented in Nextflow 23.10.0[85] with the minimal command. Briefly, FastQC
1084 (http://www.bioinformatics.babraham.ac.uk/projects/fastqc) and Trimmomatic[90] were utilized
1085 to perform quality control, and clean reads were aligned to the reference genome using
1086 Bismark[91] to account for bisulfite conversion and identify methylated cytosines. Differentially
1087 methylated sites and regions were called by the R package DSS[92] and annotated using the
1088 GENCODE VM23 dataset. Individual sites were counted as associated with a gene if located
1089 within the gene body or within 500 bp of the transcription start site (TSS). Regions were
1090 similarly annotated with a margin of 1 kb in front of the TSS. Methylation tracks were converted
1091 from mm10 to mm39 using the USCS LiftOver tool[93] for integration with RNA seq data and
1092 visualized in IGV[94]. To investigate promoter methylation in particular, the mean methylation
1093 was calculated from all covered CpG sites within 1 kbp upstream and 100 bp downstream of
1094 the TSS for genes of interest using custom Python scripts. The sequence of the promoter
1095 regions (obtained from Ensembl release 112[95]) within these limits was further analyzed for the
1096 enrichment of previously identified DNMT1-binding motifs using the AME algorithm provided
1097 within the MEME suite[96]. Gene sets of interest were analyzed for the enrichment of gene
1098 ontology terms using ShinyGO 0.80 with the biological processes' dataset[97].
1099
1100 **Chromatin immunoprecipitation (ChIP) and sequencing**
1101 Cerebellar granule cells[98] were cultured and treated as previously described[99]. DNMT1-
1102 interacting chromatin was immunoprecipitated via native chromatin immunoprecipitation
1103 (ChIP)[99]. The sequencing libraries were prepared using the NEBNext® Ultra II DNA Library
1104 Prep kit (#E7410S, New England Biolabs, U.S.A.) as per manufacturer's instructions. The input
1105 controls were pooled across samples in equimolar proportions. The libraries were amplified
1106 via PCR on a T100 Thermal Cycler (Bio-Rad, U.S.A.) with the following conditions: initial
1107 denaturation at 98°C for 30 s, 15 cycles of denaturation at 98°C for 10 s and
1108 annealing/extension at 65°C for 75 s, followed by a final extension at 65°C for 5 min. To
1109 account for the laddering caused by the enzymatic digestion, the libraries were size selected
1110 on a 2% (v/v) agarose gel and purified using the QIAquick Gel Extraction Kit (#28704, Qiagen,
1111 Germany). The libraries were sequenced on the NextSeq platform using 75 bp single-end
1112 reads at the IZKF Genomics Facility (University Hospital Aachen).
1113 FASTQ files generated from the ChIP-seq experiment were processed using the nf-
1114 core/chipseq pipeline (version 2.0.0) with the mm10 reference genome[84]. Differential peak
1115 calling between the samples was performed using THOR with default settings[100]. The identified
1116 peaks with -log10p > 1.4 in the control samples are listed in Supplementary Table 4.

1117 Sequences within a 500 bp window surrounding these peaks were analyzed for motif detection
1118 using MEME-ChIP[101].
1119
1120
1121
1122 **Single-cell RNA-sequencing**
1123 The dorsal telencephalons from E14.5 C57BL/6J mice were dissected. Single-cell
1124 suspensions were prepared using a papain dissociation system (#LK003150; Worthington
1125 Biochemical Corporation, U.S.A) and all centrifugation steps were done at 4°C. Cells were
1126 manually counted using Trypan Blue exclusion, which consistently showed a viability greater
1127 than 95%.
1128 ScRNA-seq libraries were prepared using the 10x Genomics 3' Gene Expression Kit v3.1 (10x
1129 Genomics, U.S.A). Each sample had a target of 10'000 cells and was independently loaded in
1130 the Chromium Controller (10x Genomics, U.S.A). Quality control of the cDNA and final libraries
1131 was conducted using the High Sensitivity RNA D5000 and D1000 ScreenTape assays (Agilent
1132 Technologies, U.S.A.), respectively. Libraries were pooled and sequenced on a NovaSeq 6000
1133 using the S2 Reagent Kit v1.5 with 100 cycles (Illumina, U.S.A).
1134 *FASTQ* files were processed using *CellRanger v7.0.0*. All bioinformatics analysis was
1135 performed in *R 4.4.0* running under *Ubuntu 20.04.6 LTS*. The *Seurat v5* package[102] was used
1136 for filtering, quality control, clustering, and annotation of the data. *CellChat v2.1.2*[49] was used
1137 to compute the cell communication probabilities among different clusters.
1138
1139
1140 **Neuropixels recordings and behavioral experiments**
1141 **Surgical Procedures**
1142 Mice received systemic analgesia prior to surgical procedures in form of subcutaneous
1143 injections of carprofen (4 mg/kg, Rimadyl, Zoetis GmbH, Germany) and buprenorphine
1144 (0.1 mg/kg, Buprenovet sine, Bayer Vital GMBH, Germany) and were then anesthetized using
1145 (1%–2.5%) isoflurane in oxygen. The eyes were covered with eye ointment (Bepanthen, Bayer
1146 Vital GmbH, Germany) to prevent them from drying out. Following a local injection of
1147 bupivacaine (0.08 ml of 0.25% Bucain 7.5mg/ml, Puren Pharma GmbH, Germany), the scalp
1148 was incised and pushed outward to fix it in place using tissue adhesive (Vetbond, 3M). A
1149 circular headbar was attached on top using dental cement (C&B Metabond, Parkell U.S.A.;
1150 Ortho-Jet, Lang Dental). For electrophysiological recordings, craniotomies were performed to
1151 inject a viral vector into the cortex (AAV1.shortCAG.dlox.hChR2(H134R).WPRE.hGHp, Zurich
1152 Vector Core, viral titer = ~$8x10^{12}$ vg/ml). We targeted primary somatosensory (S1) and visual
1153 (V1) cortex (stereotactic coordinates; S1: -1.5 mm anteroposterior and -3.5 mm mediolateral
1154 from Bregma; V1: -4 mm anteroposterior and -2 mm mediolateral from Bregma) and injected
1155 a volume of 200 nl in bouts of 10 nl with a 14-s delay between bouts (Nanoject III, Drummond
1156 Scientific, U.S.A.). For each coordinate, injections were performed at two cortical depths (300
1157 and 600 μm), adding up to a total volume of 400 nl per injection site. The glass pipette was
1158 removed at least 5 min after the full volume was injected to reduce the risk of backflow. After
1159 viral injections a 3-mm wide round coverslip was placed inside the craniotomy and fixed with
1160 light-curable dental cement (DE Flowable composite, Nordenta, Germany). The coverslips
1161 contained a small opening (~0.2 mm) that was covered with silicon to allow access of the

Neuropixels probes to the cortex. After the surgery, all animals received the same injections of carpofen and buprenorphine as in the beginning. They also received buprenorphine (0.009 mg/ml, Buprenovet sine, Bayer Vital GmbH, Germany) and enrofloxacin (0.0227 mg/ml, Baytril 5%, Bayer Vital GMBH, Germany) in their drinking water for three days following the surgery. Behavioral training started after at least two weeks of recovery

Neuropixels recordings

Electrophysiological recordings were done with Neuropixels 1.0 Probes in head-fixed mice, freely running on a wheel. For each mouse, we performed four recordings on consecutive days. To later recover the probe position in each recording, the probes were painted with DiD cell labeling solution (Invitrogen V22887, U.S.A.) before each recording. To record neural responses to tactile stimulation across all cortical layers, the probes were inserted at an orthogonal angle to the brain surface (~10°). The stimulation protocol was started 5–10 min after insertion, we recorded high pass-filtered data above 300 Hz at 30 kHz and low pass-filtered signals between 0.5–100 Hz at 2.5 kHz from the bottom 384 channels of the Neuropixels probe (~3.8 mm active recording area). Signals were acquired with an external Neuropixels PXIe card (IMEC, Belgium) used in a PXIe-Chassis (PXIe-1071, National Instruments, USA). Triggers and control signals for different stimuli and wheel movements were separately recorded as analog and digital signals using the SpikeGLX software (Janelia Farm Research Campus, U.S.A.; Bill Karsh).

Visual stimulation to induce gamma oscillations consisted of 5-s long full-field drifting square wave gratings at horizontal orientation and a spatial frequency of 0.04 cycles per degree. All visual stimuli were presented at a 17 cm distance from the right eye on a gamma-corrected LED-backlit LCD monitor (Viewsonic VX3276-2K-MHD-2, 32”, 60Hz refresh rate). Tactile stimulation was controlled by a microcontroller-based finite state machine (Bpod r2, Sanworks, U.S.A.) using custom Matlab code (2020b, MathWorks). Tactile stimuli consisted of 20-ms long air puffs at 0.03 bar pressure directed at the distal parts of the whiskers. In each trial, two air puffs were presented at an inter-stimulus interval of 500 ms. The overall stimulation protocol consisted of 50 tactile trials and 50 visual trials in randomized order. Inter-trial intervals were also randomized between 3–5 seconds.

To extract spiking activity, channels that were broken or outside of the brain were detected and removed from the recording using the SpikeInterface analysis toolbox. The remaining channels were time-shifted and median-subtracted across channels and time. Corrected channels were then spike-sorted with the Kilosort 2.5 software and manually curated using phy. All sorted spiking and local field potential data were analyzed using custom Matlab code (2020b, MathWorks).

Peri-event time histograms (PETHs) for sensory responses in each cluster were computed with a bin size of 10 ms and baseline-subtracted by the mean activity within 1 second before the laser onset (between 2 to 1 seconds before the first tactile stimulus). Trial-averaged local field potentials (LFPs) in response to sensory stimulation were similarly baseline-corrected. To compute current source densities (CSDs) from LFP signals, we used the inverse CSD method by Pettersen et al. (2006)[64]. We applied the spline iCSD method, assuming a smoothly varying CSD between electrode contacts, based on polynomial interpolation. We assumed a homogeneous, isotropic conductivity of $\sigma = 0.3$ S/m within and directly above the cortex[64]. To reduce spatial noise, the estimated CSD was subsequently convolved with a Gaussian spatial

filter with a standard deviation of 0.1 mm. For LFP and CSD analyses, the signals from neighboring contacts at the same depth were averaged together to improve signal quality.

Nest-building procedure

Nest-shredding and -building tests were performed with male mice between 12 and 24 weeks of age. Both *Sst-Cre* strains were tested by placing respective individuals in separate housing cages with ad libitum access to food and water but without further enrichment except for fresh bedding and standardized nest-building material (standardized autoclaved nestlets with a weight of 2–3 g (5 cm x 5 cm, Lexx, Germany). For each nestlet the weight was determined before the experiment which took place during the murine active phase (5 p.m. to 9 a.m.). After testing, all mice were transferred to their home cages and the percentual shredded material as well as the corresponding nest building score[76] were recorded.

Pentylenetetrazole (PTZ)-induced epileptic seizure protocol

Male *Sst-Cre/tdTomato* and *Sst-Cre/tdTomato/Dnmt1 LoxP*[2] mice (13- to 17-week-old) underwent an intraperitoneal administration of pentylenetetrazole (PTZ, Sigma-Aldrich, U.S.A.) with 10 mg/kg living weight. PTZ was diluted in sterile Ringer's solution (pH 7.3–7.4) to a concentration of 5 μg/μL beforehand. All mice received an intraperitoneal injection of PTZ (40 μL PTZ-solution per 20 g living weight) every ten minutes. All tested animals were monitored in transparent cages with no additional enrichment. Experiments ended as soon as the animal had a tonic-clonic seizure with significantly overstretched limbs and no further immediate recovery (event IV) or after the time limit of 150 minutes was reached. Afterwards, all mice were sacrificed with an overdose of 5% (v/v) isoflurane followed by cervical dislocation after reaching surgical tolerance, verified by loss of withdrawal response to toe pinch.

Statistics and Figure illustration

Statistical tests were performed using Matlab, Phyton, and GraphPad Prism. Unless otherwise stated, normally distributed data was tested applying unpaired and two-tailed Student's *t*-test including a subsequent Welsh's correction, two-tailed nested *t*-test, and two-way ANOVA followed by Bonferroni correction. For non-normally distributed data we used a Wilcoxon *rank-sum* test. Respective statistical tests can be found in the main text and individual captions.
Unless otherwise stated, all depicted error bars represent the standard error of the mean (SEM). Violin plots show the distribution of the numeric data using density curves, with the respective frequency of data points represented by the width. Straight lines represent the median and dotted lines the corresponding interquartile range.

References

1. Vanderhaeghen, P. & Polleux, F. Developmental mechanisms underlying the evolution of human cortical circuits. *Nat Rev Neurosci* **24**, 213–232 (2023).
2. Delaunay, D., Kawaguchi, A., Dehay, C. & Matsuzaki, F. Division modes and physical asymmetry in cerebral cortex progenitors. *Current Opinion in Neurobiology* **42**, 75–83 (2017).
3. Lin, Y. *et al.* Behavior and lineage progression of neural progenitors in the mammalian cortex. *Current Opinion in Neurobiology* **66**, 144–157 (2021).
4. Harris, K. D. & Shepherd, G. M. G. The neocortical circuit: themes and variations. *Nat Neurosci* **18**, 170–181 (2015).
5. Gerstmann, K. *et al.* Thalamic afferents influence cortical progenitors via ephrin A5-EphA4 interactions. *Development* **142**, 140–150 (2015).

6. Gerstmann, K. *et al.* A balance of noncanonical Semaphorin signaling from the cerebrospinal fluid regulates apical cell dynamics during corticogenesis. *Sci. Adv.* **8**, eabo4552 (2022).
7. Gerstmann, K. & Zimmer, G. The role of the Eph/ephrin family during cortical development and cerebral malformations. (2018).
8. Reillo, I. *et al.* A Complex Code of Extrinsic Influences on Cortical Progenitor Cells of Higher Mammals. *Cerebral Cortex* **27**, 4586–4606 (2017).
9. Villalba, A., Götz, M. & Borrell, V. The regulation of cortical neurogenesis. in *Current Topics in Developmental Biology* vol. 142 1–66 (Elsevier, 2021).
10. Kepecs, A. & Fishell, G. Interneuron cell types are fit to function. *Nature* **505**, 318–326 (2014).
11. Kessaris, N. & Denaxa, M. Cortical interneuron specification and diversification in the era of big data. *Current Opinion in Neurobiology* **80**, 102703 (2023).
12. Lim, L., Mi, D., Llorca, A. & Marín, O. Development and Functional Diversification of Cortical Interneurons. *Neuron* **100**, 294–313 (2018).
13. Wonders, C. P. & Anderson, S. A. The origin and specification of cortical interneurons. *Nat Rev Neurosci* **7**, 687–696 (2006).
14. Reichard, J. & Zimmer-Bensch, G. The Epigenome in Neurodevelopmental Disorders. *Front. Neurosci.* **15**, 776809 (2021).
15. Fogarty, M. *et al.* Spatial Genetic Patterning of the Embryonic Neuroepithelium Generates GABAergic Interneuron Diversity in the Adult Cortex. *J. Neurosci.* **27**, 10935–10946 (2007).
16. Butt, S. J. B. *et al.* The Temporal and Spatial Origins of Cortical Interneurons Predict Their Physiological Subtype. *Neuron* **48**, 591–604 (2005).
17. Niquille, M. *et al.* Neurogliaform cortical interneurons derive from cells in the preoptic area. *eLife* **7**, e32017 (2018).
18. Gelman, D. M. *et al.* The Embryonic Preoptic Area Is a Novel Source of Cortical GABAergic Interneurons. *J. Neurosci.* **29**, 9380–9389 (2009).
19. Zimmer, G. *et al.* Bidirectional ephrinB3/EphA4 signaling mediates the segregation of MGE and POA derived interneurons in the deep and superficial migratory stream. *J Neuroscience* **50**, (2011).
20. Zimmer, G. *et al.* Chondroitin Sulfate Acts in Concert with Semaphorin 3A to Guide Tangential Migration of Cortical Interneurons in the Ventral Telencephalon. *Cerebral Cortex* **20**, 2411–2422 (2010).
21. Zimmer, G. *et al.* Ephrin-A5 acts as a repulsive cue for migrating cortical interneurons. *Eur J of Neuroscience* **28**, 62–73 (2008).
22. Zimmer-Bensch, G. Diverse facets of cortical interneuron migration regulation - Implications of neuronal activity and epigenetics. *Brain research* **1700**, 160–169 (2018).
23. Lim, Y. *et al.* ARX regulates cortical interneuron differentiation and migration. Preprint at https://doi.org/10.1101/2024.01.31.578282 (2024).
24. Wang, Y. *et al.* CXCR4 and CXCR7 Have Distinct Functions in Regulating Interneuron Migration. *Neuron* **69**, 61–76 (2011).
25. Bartolini, G. *et al.* Neuregulin 3 Mediates Cortical Plate Invasion and Laminar Allocation of GABAergic Interneurons. *Cell Reports* **18**, 1157–1170 (2017).
26. Yildiz, C. B. & Zimmer-Bensch, G. Role of DNMTs in the Brain. *Adv Exp Med Biol* **1389**, 363–394 (2022).
27. Pensold, D. *et al.* The DNA Methyltransferase 1 (DNMT1) Controls the Shape and Dynamics of Migrating POA-Derived Interneurons Fated for the Murine Cerebral Cortex. *Cereb Cortex* **27**, 5696–5714 (2017).
28. Urban-Ciecko, J. & Barth, A. L. Somatostatin-expressing neurons in cortical networks. *Nat Rev Neurosci* **17**, 401–409 (2016).
29. Liodis, P. *et al. Lhx6* Activity Is Required for the Normal Migration and Specification of Cortical Interneuron Subtypes. *J. Neurosci.* **27**, 3078–3089 (2007).
30. Lim, L. *et al.* Optimization of interneuron function by direct coupling of cell migration and axonal targeting. *Nat Neurosci* **21**, 920–931 (2018).
31. Hu, J. S., Vogt, D., Sandberg, M. & Rubenstein, J. L. Cortical interneuron

development: a tale of time and space. *Development* **144**, 3867–3878 (2017).
32. Bock, C. Analysing and interpreting DNA methylation data. *Nat Rev Genet* **13**, 705–719 (2012).
33. Lister, R. *et al.* Human DNA methylomes at base resolution show widespread epigenomic differences. *Nature* **462**, 315–322 (2009).
34. Mayer, C. *et al.* Developmental diversification of cortical inhibitory interneurons. *Nature* **555**, 457–462 (2018).
35. Gruner, H. N., Kim, M. & Mastick, G. S. Robo1 and 2 Repellent Receptors Cooperate to Guide Facial Neuron Cell Migration and Axon Projections in the Embryonic Mouse Hindbrain. *Neuroscience* **402**, 116–129 (2019).
36. Talebian, A. *et al.* Autonomous and non-autonomous roles for ephrin-B in interneuron migration. *Developmental Biology* **431**, 179–193 (2017).
37. Marín, O., Yaron, A., Bagri, A., Tessier-Lavigne, M. & Rubenstein, J. L. Sorting of striatal and cortical interneurons regulated by semaphorin-neuropilin interactions. *Science* **293**, 872–875 (2001).
38. Gabel, H. W. *et al.* Disruption of DNA-methylation-dependent long gene repression in Rett syndrome. *Nature* **522**, 89–93 (2015).
39. Nan, X. *et al.* Transcriptional repression by the methyl-CpG-binding protein MeCP2 involves a histone deacetylase complex. *Nature* **393**, 386–389 (1998).
40. Boyes, J. & Bird, A. DNA methylation inhibits transcription indirectly via a methyl-CpG binding protein. *Cell* **64**, 1123–1134 (1991).
41. Pensold, D. *et al.* DNA Methylation-Mediated Modulation of Endocytosis as Potential Mechanism for Synaptic Function Regulation in Murine Inhibitory Cortical Interneurons. *Cereb Cortex* **30**, 3921–3937 (2020).
42. Batista-Brito, R. *et al.* The Cell-Intrinsic Requirement of Sox6 for Cortical Interneuron Development. *Neuron* **63**, 466–481 (2009).
43. van den Berghe, V. *et al.* Directed Migration of Cortical Interneurons Depends on the Cell-Autonomous Action of Sip1. *Neuron* **77**, 70–82 (2013).
44. McKinsey, G. L. *et al.* Dlx1&2-Dependent Expression of Zfhx1b (Sip1, Zeb2) Regulates the Fate Switch between Cortical and Striatal Interneurons. *Neuron* **77**, 83–98 (2013).
45. Fisher, J. *et al.* Cortical somatostatin long-range projection neurons and interneurons exhibit divergent developmental trajectories. *Neuron* **112**, 558-573.e8 (2024).
46. Sessa, A. *et al.* Tbr2-positive intermediate (basal) neuronal progenitors safeguard cerebral cortex expansion by controlling amplification of pallial glutamatergic neurons and attraction of subpallial GABAergic interneurons. *Genes Dev.* **24**, 1816–1826 (2010).
47. Silva, C. G. *et al.* Cell-Intrinsic Control of Interneuron Migration Drives Cortical Morphogenesis. *Cell* **172**, 1063-1078.e19 (2018).
48. Kischel, A., Audouard, C., Fawal, M.-A. & Davy, A. Ephrin-B2 paces neuronal production in the developing neocortex. *BMC Dev Biol* **20**, 12 (2020).
49. Jin, S. *et al.* Inference and analysis of cell-cell communication using CellChat. *Nat Commun* **12**, 1088 (2021).
50. Hevner, R. F. *et al.* Tbr1 Regulates Differentiation of the Preplate and Layer 6. *Neuron* **29**, 353–366 (2001).
51. Bulfone, A. *et al.* T-Brain-1: A homolog of Brachyury whose expression defines molecularly distinct domains within the cerebral cortex. *Neuron* **15**, 63–78 (1995).
52. Vasistha, N. A. *et al.* Cortical and Clonal Contribution of Tbr2 Expressing Progenitors in the Developing Mouse Brain. *Cereb. Cortex* **25**, 3290–3302 (2015).
53. Kowalczyk, T. *et al.* Intermediate neuronal progenitors (basal progenitors) produce pyramidal-projection neurons for all layers of cerebral cortex. *Cereb Cortex* **19**, 2439–2450 (2009).
54. Mihalas, A. B. *et al.* Intermediate Progenitor Cohorts Differentially Generate Cortical Layers and Require Tbr2 for Timely Acquisition of Neuronal Subtype Identity. *Cell Reports* **16**, 92–105 (2016).
55. Harrison-Uy, S. J. & Pleasure, S. J. Wnt Signaling and Forebrain Development. *Cold Spring Harbor Perspectives in Biology* **4**, a008094–a008094 (2012).

56. Nian, F.-S. & Hou, P.-S. Evolving Roles of Notch Signaling in Cortical Development. *Front. Neurosci.* **16**, 844410 (2022).
57. Cárdenas, A. *et al.* Evolution of Cortical Neurogenesis in Amniotes Controlled by Robo Signaling Levels. *Cell* **174**, 590-606.e21 (2018).
58. Smith, A., Robinson, V., Patel, K. & Wilkinson, D. G. The EphA4 and EphB1 receptor tyrosine kinases and ephrin-B2 ligand regulate targeted migration of branchial neural crest cells. *Current Biology* **7**, 561–570 (1997).
59. Riedemann, T. Diversity and Function of Somatostatin-Expressing Interneurons in the Cerebral Cortex. *IJMS* **20**, 2952 (2019).
60. Ward, C. *et al.* Developmental Disruption of Mef2c in Medial Ganglionic Eminence–Derived Cortical Inhibitory Interneurons Impairs Cellular and Circuit Function. *Biological Psychiatry* S000632232401360X (2024) doi:10.1016/j.biopsych.2024.05.021.
61. Allaway, K. C. *et al.* Genetic and epigenetic coordination of cortical interneuron development. *Nature* **597**, 693–697 (2021).
62. Pai, E. L.-L. *et al.* Maf and Mafb control mouse pallial interneuron fate and maturation through neuropsychiatric disease gene regulation. *eLife* **9**, e54903 (2020).
63. Musall, S., Kaufman, M. T., Juavinett, A. L., Gluf, S. & Churchland, A. K. Single-trial neural dynamics are dominated by richly varied movements. *Nat Neurosci* **22**, 1677–1686 (2019).
64. Pettersen, K. H., Devor, A., Ulbert, I., Dale, A. M. & Einevoll, G. T. Current-source density estimation based on inversion of electrostatic forward solution: Effects of finite extent of neuronal activity and conductivity discontinuities. *Journal of Neuroscience Methods* **154**, 116–133 (2006).
65. Petersen, C. C. H. The Functional Organization of the Barrel Cortex. *Neuron* **56**, 339–355 (2007).
66. Fries, P., Reynolds, J. H., Rorie, A. E. & Desimone, R. Modulation of Oscillatory Neuronal Synchronization by Selective Visual Attention. *Science* **291**, 1560–1563 (2001).
67. Veit, J., Hakim, R., Jadi, M. P., Sejnowski, T. J. & Adesnik, H. Cortical gamma band synchronization through somatostatin interneurons. *Nat Neurosci* **20**, 951–959 (2017).
68. Ahnaou, A., Huysmans, H., Van De Casteele, T. & Drinkenburg, W. H. I. M. Cortical high gamma network oscillations and connectivity: a translational index for antipsychotics to normalize aberrant neurophysiological activity. *Transl Psychiatry* **7**, 1285 (2017).
69. Yamamoto, J., Suh, J., Takeuchi, D. & Tonegawa, S. Successful Execution of Working Memory Linked to Synchronized High-Frequency Gamma Oscillations. *Cell* **157**, 845–857 (2014).
70. Kas, M. J. H., Fernandes, C., Schalkwyk, L. C. & Collier, D. A. Genetics of behavioural domains across the neuropsychiatric spectrum; of mice and men. *Mol Psychiatry* **12**, 324–330 (2007).
71. Liguz-Lecznar, M., Dobrzanski, G. & Kossut, M. Somatostatin and Somatostatin-Containing Interneurons—From Plasticity to Pathology. *Biomolecules* **12**, 312 (2022).
72. Jirkof, P. Burrowing and nest building behavior as indicators of well-being in mice. *Journal of Neuroscience Methods* **234**, 139–146 (2014).
73. Perry, G., Brindley, L. M., Muthukumaraswamy, S. D., Singh, K. D. & Hamandi, K. Evidence for increased visual gamma responses in photosensitive epilepsy. *Epilepsy Research* **108**, 1076–1086 (2014).
74. Mandhane, S. N., Aavula, K. & Rajamannar, T. Timed pentylenetetrazol infusion test: A comparative analysis with s.c.PTZ and MES models of anticonvulsant screening in mice. *Seizure* **16**, 636–644 (2007).
75. Chenn, A. & Walsh, C. A. Regulation of Cerebral Cortical Size by Control of Cell Cycle Exit in Neural Precursors. *Science* **297**, 365–369 (2002).
76. Deacon, R. M. Assessing nest building in mice. *Nat Protoc* **1**, 1117–1119 (2006).
77. Madisen, L. *et al.* A robust and high-throughput Cre reporting and characterization system for the whole mouse brain. *Nat Neurosci* **13**, 133–40 (2010).
78. Jackson-Grusby, L. *et al.* Loss of genomic methylation causes p53-dependent apoptosis and epigenetic deregulation. *Nat Genet* **27**, 31–39 (2001).
79. Symmank, J., Gölling, V., Gerstmann, K. & Zimmer, G. The Transcription Factor

LHX1 Regulates the Survival and Directed Migration of POA-derived Cortical Interneurons. *Cereb Cortex* **29**, 1644–1658 (2019).
80. Hahn, A. *et al.* DNA Methyltransferase 1 (DNMT1) Function Is Implicated in the Age-Related Loss of Cortical Interneurons. *Frontiers in cell and developmental biology* **8**, 639 (2020).
81. Schindelin, J. *et al.* Fiji: an open-source platform for biological-image analysis. *Nat Methods* **9**, 676–682 (2012).
82. Saxena, S., Maroju, P. A., Choudhury, S., Anne, A. & Mohan, K. N. Analysis of transcript levels of a few schizophrenia candidate genes in neurons from a transgenic mouse embryonic stem cell model overexpressing DNMT1. *Gene* **757**, 144934 (2020).
83. Singh, M., Saxena, S. & Mohan, K. N. DNMT1 downregulation as well as its overexpression distinctly affect mostly overlapping genes implicated in schizophrenia, autism spectrum, epilepsy, and bipolar disorders. *Front. Mol. Neurosci.* **16**, 1275697 (2023).
84. Ewels, P. A. *et al.* The nf-core framework for community-curated bioinformatics pipelines. *Nat Biotechnol* **38**, 276–278 (2020).
85. Di Tommaso, P. *et al.* Nextflow enables reproducible computational workflows. *Nat Biotechnol* **35**, 316–319 (2017).
86. Krueger, F., James, F., Ewels, P., Afyounian, E. & Schuster-Boeckler, B. FelixKrueger/TrimGalore: v0.6.7 - DOI via Zenodo. Zenodo https://doi.org/10.5281/ZENODO.5127899 (2021).
87. Dobin, A. *et al.* STAR: ultrafast universal RNA-seq aligner. *Bioinformatics* **29**, 15–21 (2013).
88. Patro, R., Duggal, G., Love, M. I., Irizarry, R. A. & Kingsford, C. Salmon provides fast and bias-aware quantification of transcript expression. *Nat Methods* **14**, 417–419 (2017).
89. Love, M. I., Huber, W. & Anders, S. Moderated estimation of fold change and dispersion for RNA-seq data with DESeq2. *Genome Biol* **15**, 550 (2014).
90. Bolger, A. M., Lohse, M. & Usadel, B. Trimmomatic: a flexible trimmer for Illumina sequence data. *Bioinformatics* **30**, 2114–2120 (2014).
91. Krueger, F. & Andrews, S. R. Bismark: a flexible aligner and methylation caller for Bisulfite-Seq applications. *Bioinformatics* **27**, 1571–1572 (2011).
92. Feng, H., Conneely, K. N. & Wu, H. A Bayesian hierarchical model to detect differentially methylated loci from single nucleotide resolution sequencing data. *Nucleic Acids Research* **42**, e69–e69 (2014).
93. Hinrichs, A. S. The UCSC Genome Browser Database: update 2006. *Nucleic Acids Research* **34**, D590–D598 (2006).
94. Robinson, J. T. *et al.* Integrative genomics viewer. *Nat Biotechnol* **29**, 24–26 (2011).
95. Harrison, P. W. *et al.* Ensembl 2024. *Nucleic Acids Res* **52**, D891–D899 (2024).
96. Buske, F. A., Bodén, M., Bauer, D. C. & Bailey, T. L. Assigning roles to DNA regulatory motifs using comparative genomics. *Bioinformatics* **26**, 860–866 (2010).
97. Ge, S. X., Jung, D. & Yao, R. ShinyGO: a graphical gene-set enrichment tool for animals and plants. *Bioinformatics* **36**, 2628–2629 (2020).
98. Fossale, E. *et al.* Membrane trafficking and mitochondrial abnormalities precede subunit c deposition in a cerebellar cell model of juvenile neuronal ceroid lipofuscinosis. *BMC Neurosci* **5**, 57 (2004).
99. Yildiz, C. B. *et al.* EphrinA5 regulates cell motility by modulating Snhg15/DNA triplex-dependent targeting of DNMT1 to the Ncam1 promoter. *Epigenetics & Chromatin* **16**, 42 (2023).
100. Allhoff, M., Seré, K., F Pires, J., Zenke, M. & G Costa, I. Differential peak calling of ChIP-seq signals with replicates with THOR. *Nucleic Acids Res* **44**, e153 (2016).
101. Machanick, P. & Bailey, T. L. MEME-ChIP: motif analysis of large DNA datasets. *Bioinformatics* **27**, 1696–1697 (2011).
102. Hao, Y. *et al.* Dictionary learning for integrative, multimodal and scalable single-cell analysis. *Nat Biotechnol* (2023) doi:10.1038/s41587-023-01767-y.

Main Figures

Figure 1:

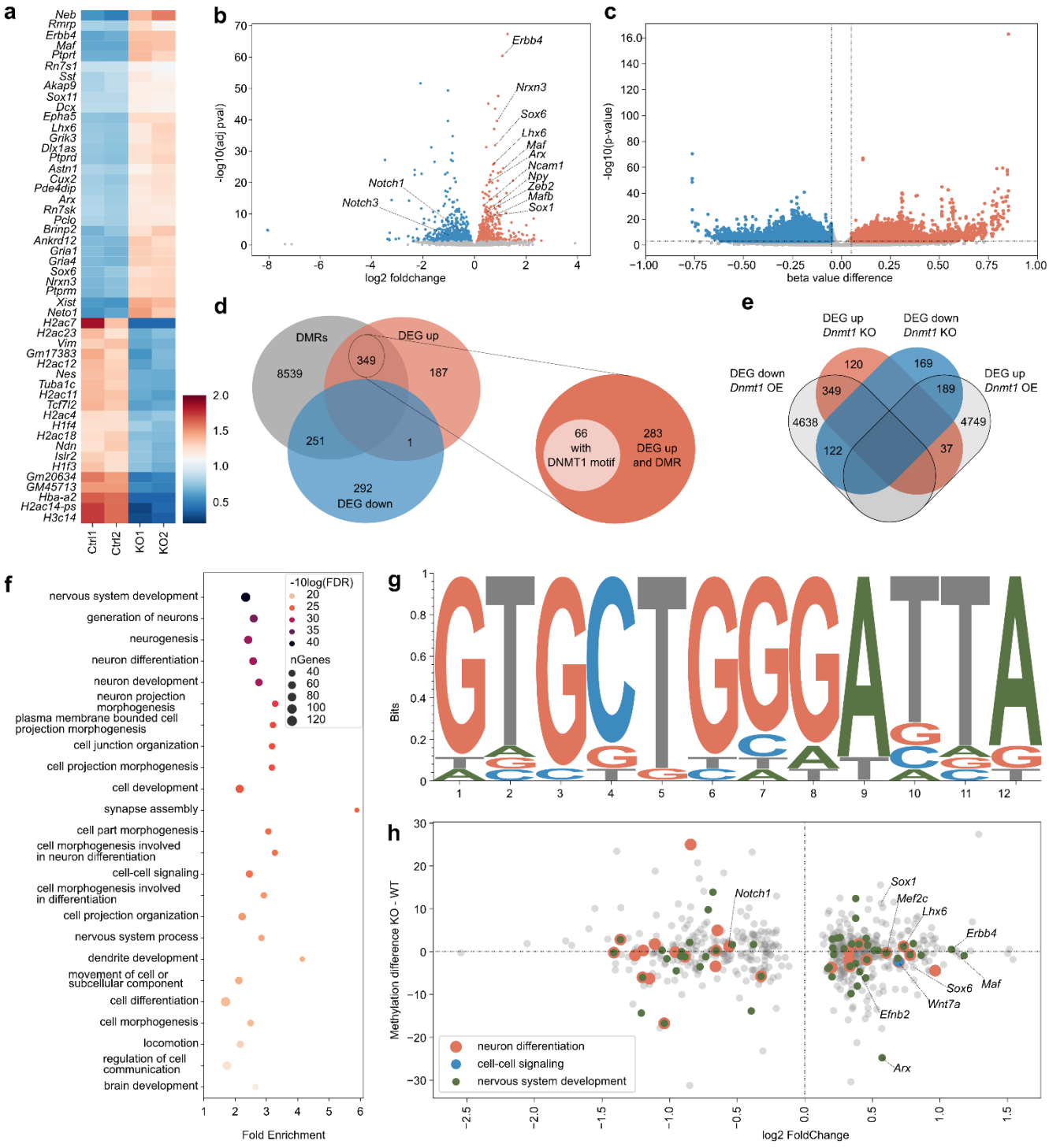
a
Neb
Rmrp
Erbb4
Maf
Ptprt
Rn7s1
Sst
Akap9
Sox11
Dcx
Epha5
Lhx6
Grik3
Dlx1as
Ptprd
Astn1
Cux2
Pde4dip
Arx
Rn7sk
Pclo
Brinp2
Ankrd12
Gria1
Gria4
Sox6
Nrxn3
Ptprm
Xist
Neto1
H2ac7
H2ac23
Vim
Gm17383
H2ac12
Nes
Tuba1c
H2ac11
Tcf7l2
H2ac4
H1f4
H2ac18
Ndn
Islr2
H1f3
Gm20634
GM45713
Hba-a2
H2ac14-ps
H3c14
Ctrl1
Ctrl2
KO1
KO2
b
-log10(adj pval)
log2 foldchange
Erbb4
Nrxn3
Sox6
Lhx6
Maf
Arx
Ncam1
Npy
Zeb2
Mafb
Sox1
Notch1
Notch3
c
-log10(p-value)
beta value difference
d
DMRs
DEG up
DEG down
8539
349
187
251
1
292
66 with DNMT1 motif
283 DEG up and DMR
e
DEG up Dnmt1 KO
DEG down Dnmt1 KO
DEG down Dnmt1 OE
DEG up Dnmt1 OE
120
169
349
189
4638
4749
122
37
f
-10log(FDR)
nGenes
nervous system development
generation of neurons
neurogenesis
neuron differentiation
neuron development
neuron projection morphogenesis
plasma membrane bounded cell projection morphogenesis
cell junction organization
cell projection morphogenesis
cell development
synapse assembly
cell part morphogenesis
cell morphogenesis involved in neuron differentiation
cell-cell signaling
cell morphogenesis involved in differentiation
cell projection organization
nervous system process
dendrite development
movement of cell or subcellular component
cell differentiation
cell morphogenesis
locomotion
regulation of cell communication
brain development
Fold Enrichment
g
Bits
h
Methylation difference KO - WT
log2 FoldChange
Notch1
Sox1
Mef2c
Lhx6
Erbb4
Maf
Sox6
Wnt7a
Efnb2
Arx
neuron differentiation
cell-cell signaling
nervous system development
i
Arx
Lhx6
Satb1
Zeb2
Maf
Mafb
Efnb2
Sox6
Sox1
Methylation difference KO -Ctrl
-0.18
-0.12
-0.06
0.00
0.06
distance to TSS
j
15 kb
92.330 kb
92.332 kb
92.334 kb
92.336 kb
92.338 kb
92.340 kb
92.342 kb
Ctrl RNAseq
KO RNAseq
Ctrl Methylation
KO Methylation
DMRs
Refseq Genes
Arx

Figure 2

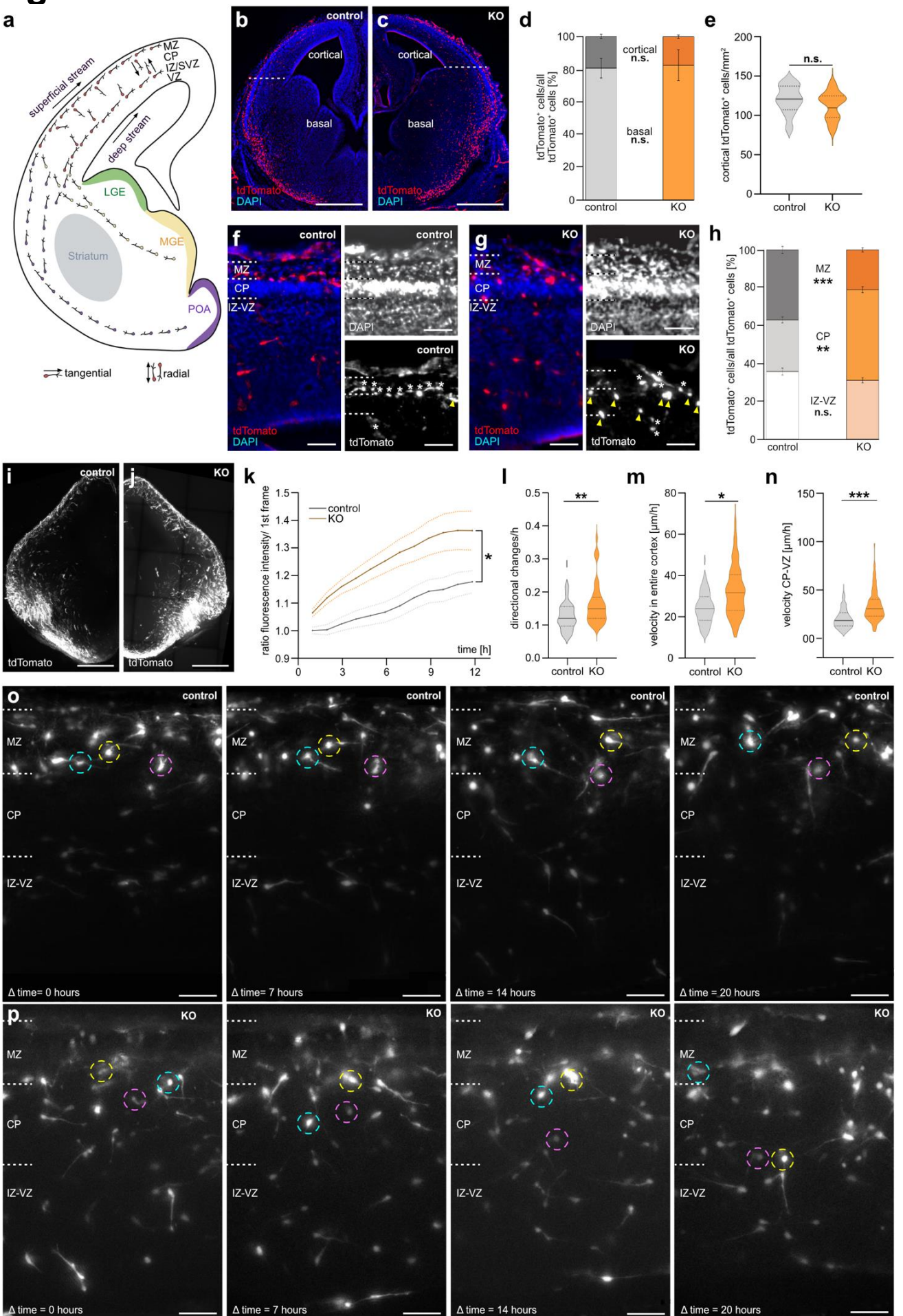
a
superficial stream
deep stream
MZ
CP
IZ/SVZ
VZ
LGE
MGE
Striatum
POA
tangential
radial
b
control
cortical
basal
tdTomato
DAPI
c
KO
cortical
basal
tdTomato
DAPI
d
tdTomato+ cells/all tdTomato+ cells [%]
cortical
n.s.
basal
n.s.
control
KO
e
cortical tdTomato+ cells/mm2
n.s.
control
KO
f
control
MZ
CP
IZ-VZ
tdTomato
DAPI
DAPI
tdTomato
g
KO
MZ
CP
IZ-VZ
tdTomato
DAPI
DAPI
tdTomato
h
tdTomato+ cells/all tdTomato+ cells [%]
MZ
***
CP
**
IZ-VZ
n.s.
control
KO
i
control
tdTomato
j
KO
tdTomato
k
ratio fluorescence intensity/ 1st frame
control
KO
*
time [h]
l
directional changes/h
**
control
KO
m
velocity in entire cortex [µm/h]
*
control
KO
n
velocity CP-VZ [µm/h]
***
control
KO
o
control
MZ
CP
IZ-VZ
Δ time= 0 hours
Δ time= 7 hours
Δ time = 14 hours
Δ time = 20 hours
p
KO
MZ
CP
IZ-VZ
Δ time = 0 hours
Δ time = 7 hours
Δ time = 14 hours
Δ time = 20 hours

Figure 3

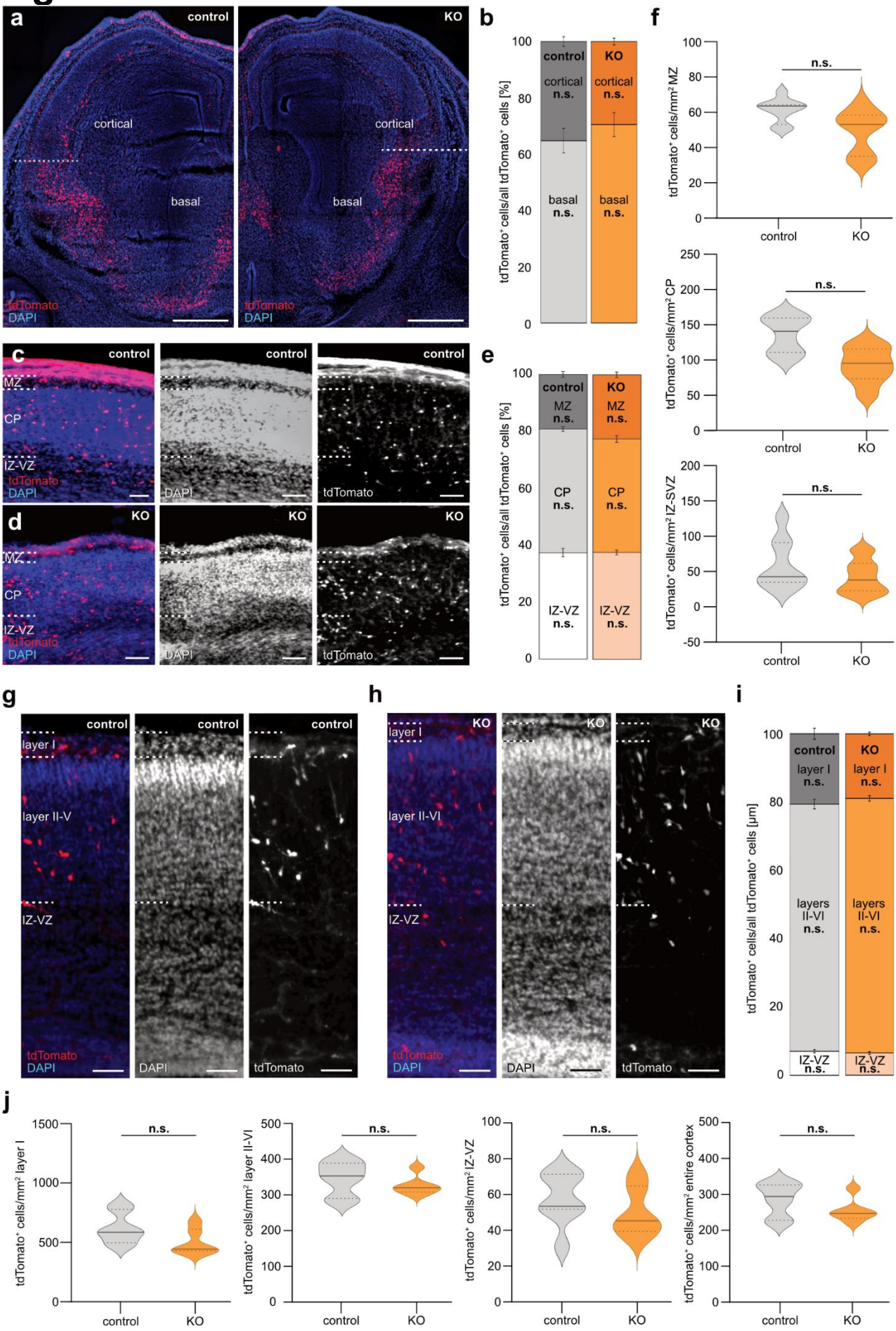
a
control
KO
cortical
basal
tdTomato
DAPI
b
tdTomato+ cells/all tdTomato+ cells [%]
control
KO
cortical n.s.
basal n.s.
c
d
MZ
CP
IZ-VZ
e
MZ n.s.
CP n.s.
IZ-VZ n.s.
f
tdTomato+ cells/mm² MZ
tdTomato+ cells/mm² CP
tdTomato+ cells/mm² IZ-SVZ
n.s.
g
layer I
layer II-V
h
layer II-VI
i
tdTomato+ cells/all tdTomato+ cells [µm]
layer I n.s.
layers II-VI n.s.
IZ-VZ n.s.
j
tdTomato+ cells/mm² layer I
tdTomato+ cells/mm² layer II-VI
tdTomato+ cells/mm² IZ-VZ
tdTomato+ cells/mm² entire cortex

Figure 4

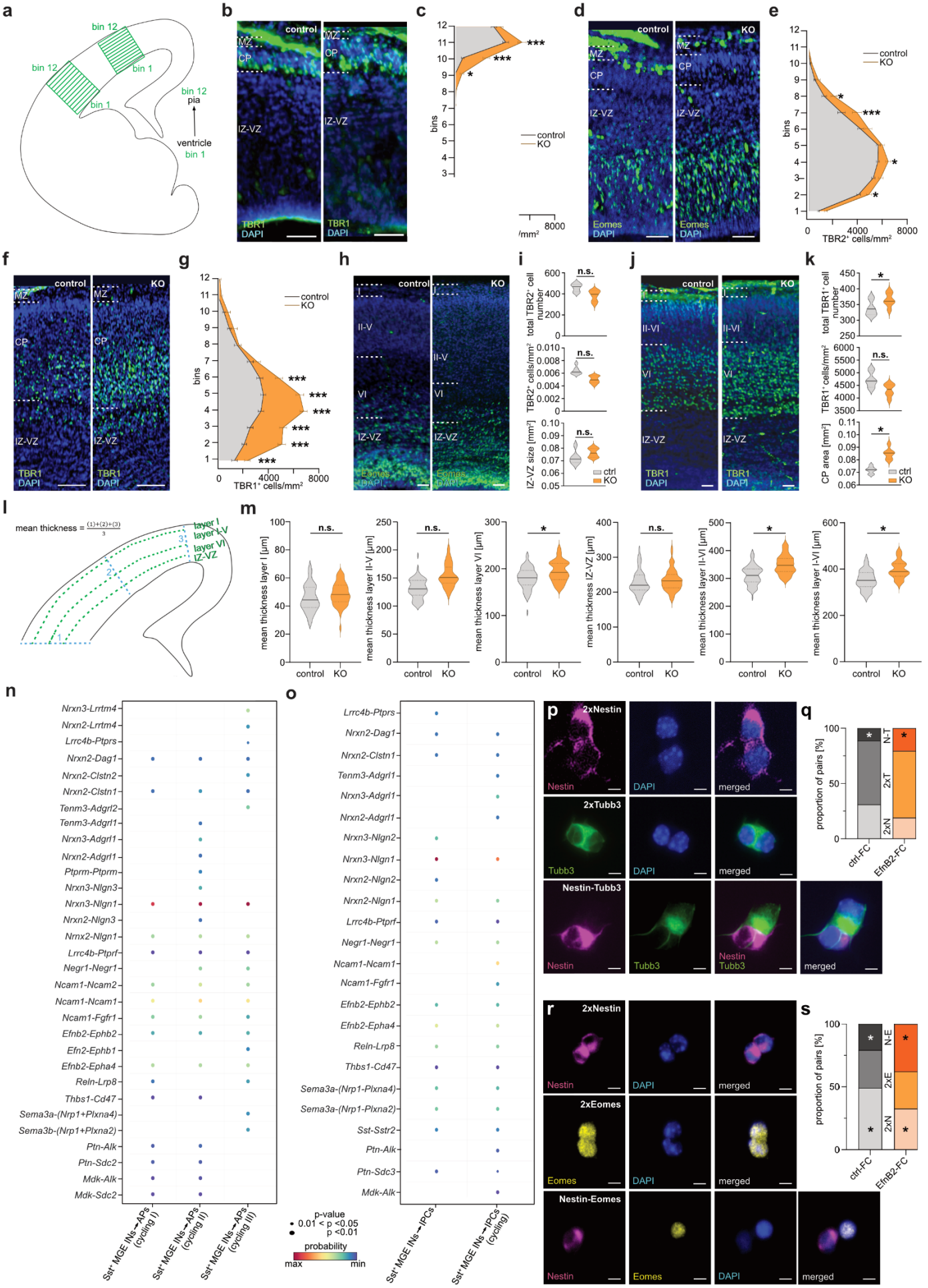
a
bin 12
bin 12
bin 1
bin 1
bin 12
pia
ventricle
bin 1
b
control
KO
MZ
CP
IZ-VZ
TBR1
DAPI
c
bins
control
KO
8000
/mm²
d
control
KO
MZ
CP
IZ-VZ
Eomes
DAPI
e
control
KO
bins
TBR2⁺ cells/mm²
f
control
KO
MZ
CP
IZ-VZ
TBR1
DAPI
g
control
KO
bins
TBR1⁺ cells/mm²
h
control
KO
I
II-V
VI
IZ-VZ
Eomes
DAPI
i
total TBR2⁺ cell number
TBR2⁺ cells/mm²
IZ-VZ size [mm²]
n.s.
ctrl
KO
j
control
KO
I
II-VI
VI
IZ-VZ
TBR1
DAPI
k
total TBR1⁺ cell number
TBR1⁺ cells/mm²
CP area [mm²]
n.s.
ctrl
KO
l
mean thickness = (1)+(2)+(3) / 3
layer I
layer II-V
layer VI
IZ-VZ
m
mean thickness layer I [µm]
mean thickness layer II-V [µm]
mean thickness layer VI [µm]
mean thickness IZ-VZ [µm]
mean thickness layer II-VI [µm]
mean thickness layer I-VI [µm]
n.s.
control
KO
n
Nrxn3-Lrrtm4
Nrxn2-Lrrtm4
Lrrc4b-Ptprs
Nrxn2-Dag1
Nrxn2-Clstn2
Nrxn2-Clstn1
Tenm3-Adgrl2
Tenm3-Adgrl1
Nrxn3-Adgrl1
Nrxn2-Adgrl1
Ptprm-Ptprm
Nrxn3-Nlgn3
Nrxn3-Nlgn1
Nrxn2-Nlgn3
Nrnx2-Nlgn1
Lrrc4b-Ptprf
Negr1-Negr1
Ncam1-Ncam2
Ncam1-Ncam1
Ncam1-Fgfr1
Efnb2-Ephb2
Efn2-Ephb1
Efnb2-Epha4
Reln-Lrp8
Thbs1-Cd47
Sema3a-(Nrp1+Plxna4)
Sema3b-(Nrp1+Plxna2)
Ptn-Alk
Ptn-Sdc2
Mdk-Alk
Mdk-Sdc2
Sst⁺ MGE INs→APs (cycling I)
Sst⁺ MGE INs→APs (cycling II)
Sst⁺ MGE INs→APs (cycling III)
o
Lrrc4b-Ptprs
Nrxn2-Dag1
Nrxn2-Clstn1
Tenm3-Adgrl1
Nrxn3-Adgrl1
Nrxn2-Adgrl1
Nrxn3-Nlgn2
Nrxn3-Nlgn1
Nrxn2-Nlgn2
Nrxn2-Nlgn1
Lrrc4b-Ptprf
Negr1-Negr1
Ncam1-Ncam1
Ncam1-Fgfr1
Efnb2-Ephb2
Efnb2-Epha4
Reln-Lrp8
Thbs1-Cd47
Sema3a-(Nrp1-Plxna4)
Sema3a-(Nrp1-Plxna2)
Sst-Sstr2
Ptn-Alk
Ptn-Sdc3
Mdk-Alk
Sst⁺ MGE INs→IPCs
Sst⁺ MGE INs→IPCs (cycling)
p-value
0.01 < p <0.05
p <0.01
probability
max
min
p
2xNestin
Nestin
DAPI
merged
2xTubb3
Tubb3
Nestin-Tubb3
q
proportion of pairs [%]
N-T
2xT
2xN
ctrl-FC
EfnB2-FC
r
2xNestin
2xEomes
Eomes
Nestin-Eomes
s
proportion of pairs [%]
N-E
2xE
2xN
ctrl-FC
EfnB2-FC

Figure 5

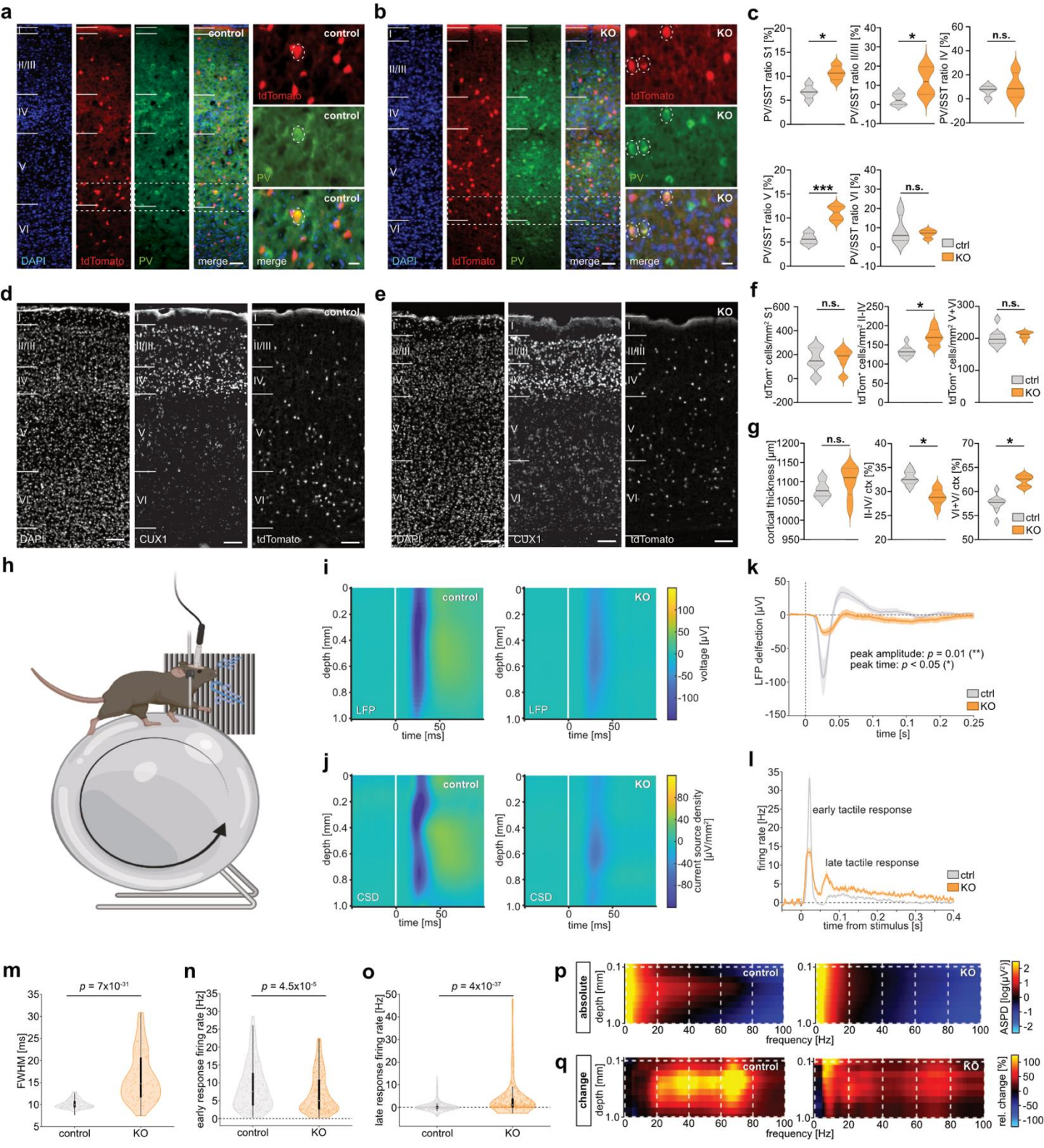
a
b
c
d
e
f
g
h
i
j
k
l
m
n
o
p
q
control
KO
tdTomato
PV
merge
DAPI
CUX1
I
II/III
IV
V
VI
PV/SST ratio S1 [%]
PV/SST ratio II/III [%]
PV/SST ratio IV [%]
PV/SST ratio V [%]
PV/SST ratio VI [%]
n.s.
ctrl
tdTom+ cells/mm² S1
tdTom+ cells/mm² II-IV
tdTom+ cells/mm² V+VI
cortical thickness [µm]
II-IV/ ctx [%]
VI+V/ ctx [%]
LFP
CSD
depth [mm]
time [ms]
voltage [µV]
current source density [µV/mm²]
LFP deflection [µV]
peak amplitude: p = 0.01 (**)
peak time: p < 0.05 (*)
time [s]
early tactile response
late tactile response
firing rate [Hz]
time from stimulus [s]
FWHM [ms]
p = 7x10-31
early response firing rate [Hz]
p = 4.5x10-5
late response firing rate [Hz]
p = 4x10-37
absolute
change
frequency [Hz]
ASPD [log(µV²)]
rel. change [%]

Figure 6

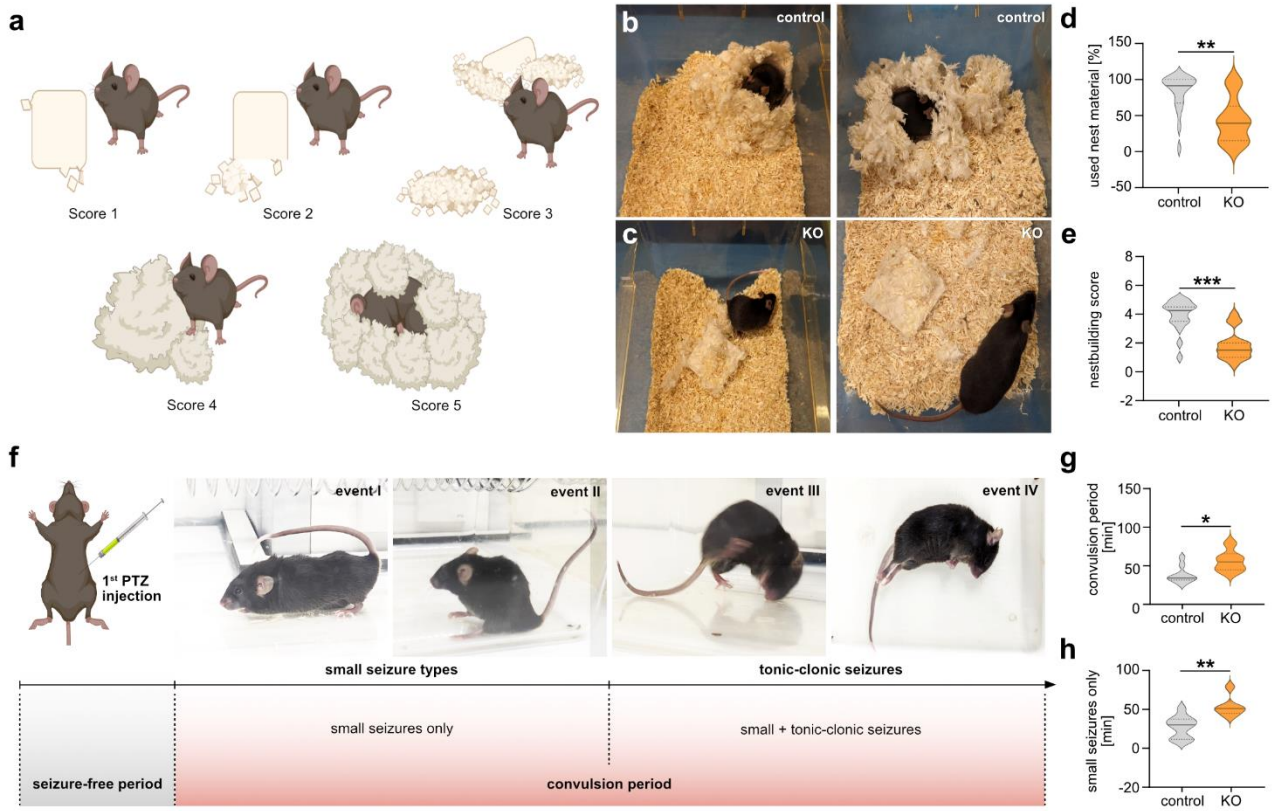
a
Score 1
Score 2
Score 3
Score 4
Score 5
b
control
control
c
KO
KO
d
used nest material [%]
150
100
50
0
-50
**
control
KO
e
nestbuilding score
8
6
4
2
0
-2
***
control
KO
f
1st PTZ injection
event I
event II
event III
event IV
small seizure types
tonic-clonic seizures
small seizures only
small + tonic-clonic seizures
seizure-free period
convulsion period
g
convulsion period [min]
150
100
50
0
*
control
KO
h
small seizures only [min]
100
50
0
-20
**
control
KO

Extended Data Figure Legends

Extended Data Figure E1:

Validation of SST expression and reduced DNMT1 levels in tdTomato-positive cells. (a) Mating strategy to obtain *Sst-Cre/tdTomato* (control) and *Sst-Cre/tdTomato/Dnmt1 loxP*^{2} (KO) mice. *Sst*$^{tm2.l(cre)Zjh}$/J mice were mated with *tdTomato* reporter mice (*B6.CgGt(ROSA)26Sor*$^{tml\ 4(CAG\text{-}tdTomato)Hze}$) resulting in *Sst-Cre/tdTomato* mice with an internal ribosomal entry site (*IRES*), a *Cre-recombinase* sequence, a *polyA* sequence, and a *frt*-flanked neo cassette located in the 3' untranslated region (UTR) of the *Somatostatin* (*Sst*) locus on chromosome 16, limiting the respective *Cre* expression to *Sst*-positive neurons. The *tdTomato* sequence and a loxP-flanked stop cassette are located in the *Rosa26* locus. Triple transgenic *Sst-Cre/tdTomato/Dnmt1 loxP*^{2} mice were obtained by crossing control mice with a *Dnmt1 loxP*^{2} strain (*B6; 129Sv-Dnmt1tm4Jae/J*; exon 4 and 5 of the *Dnmt1* gene are *loxP*-flanked, resulting in a null allele of these loci and a subsequent DNMT1 deficiency. **(b)** Exemplary microphotographs depicting SST expression in tdTomato-cells in sagittalbrain sections of a four-month-old male *Sst-Cre/tdTomato* mouse (Bregma 2.76). **(c)** Magnified images of the areas outlined in b. Scale bars: 100 μm in b and 20 μm c. **(d-g)** Quantification of DNMT1 expression by immunohistochemistry in *Dnmt1*-control **(d, e)** and *Dnmt1*-KO **(f, g)** male mice (six-month-old individuals) in 30 μm, fixated coronal cryosections. Scale bars **(d, f)** 100 μm and 10 μm **(e,g)**. **(h)** Quantification of the ratio of DNMT1-positive to DNMT1-negative *tdTomato*-expressing cells (Bregma 1.18, 1.10, 0.14, -0.22, -2.92. -3.08, -3.28 were used for quantification). Two-tailed nested *t*-test, ($p < 0.001$ ***, $N = 3$ for *Sst-Cre/tdTomato* ($n = 18$ slices) and *Sst-Cre/tdTomato/Dnmt1 loxP*^{2} ($n = 17$ slices), respectively.

Extended Data Figure E2:

Characteristics of genes that were upregulated in expression as well as differentially methylated in FAC-sorted *Sst-Cre/tdTomato/Dnmt1 loxP*^{2} neurons compared to *Sst-Cre/tdTomato* cells at E14.5 compared with the rest in the genome; Chi-squared and Student's *t*-tests were run to analyze if our gene set has special characteristics when compared with all the other genes (ShinyGO 0.80; http://bioinformatics.sdstate.edu/go/). **(a)** Gene ontology (GO), **(b)** bar plots, and **(c)** density plots.

Extended Data Figure E3:

(a) Gene ontology (GO) analysis for the set of genes that were upregulated in expression in *Sst*-positive neurons of *Sst-Cre/tdTomato/Dnmt1 loxP*^{2} mice compared to *Sst-Cre/tdTomato* at E14.5. **(b)** Further characteristics are shown in bar plots (tested by Chi-squared test) and density plots **(c),** depicting the characteristics of this gene set compared with the entire set of detected transcripts (Student's *t*-tests).

Extended Data Figure E4:

RNA sequencing tracks combined with methylation profile for select genes obtained from FAC-sorted cells of *Sst-Cre/tdTomato* and *Sst-Cre/tdTomato/Dnmt1 loxP*^{2} mice (E14.5). Forward and reverse tracks from both RNA sequencing runs were combined into one track per genotype. Similarly, both methylation tracks per genotype were combined. Differentially methylated regions identified by DSS are indicated below. Tracks were illustrated with IGV viewer V2.17.2, refseq mm39.

Extended Data Figure E5:

The genes upregulated in *Sst*-expressing interneurons of *Sst-Cre/tdTomato/Dnmt1-loxP*^{2} mice partially overlap with genes that are downregulated after *Dnmt1* overexpression in neurons obtained from murine embryonic stem cells (ESCs). **(a)** Gene ontology (GO) analysis for the overlap. **(b)** Further characteristics are shown in bar plots (tested by Chi-squared test) and density plots **(c)**, depicting the characteristics of this gene set compared with the entire set of detected transcripts (Student's *t*-tests).

Extended Data Figure E6:

(a-c) ErbB4 level is increased after *Dnmt1* knockdown (KD) in MGE cells (E14.5 + 1div). Exemplary microphotographs showing control siRNA-treated (a) and *Dnmt1*-KD cells (b) stained for Phalloidin-647 and ErbB4. On the very right of each example, thermal-color-coded panels represent the respective fluorescent intensity of ErbB4 (therm. (thermal) LUT). A dark blue color indicates 0 and a red color represents 5000 fluorescent units. Scale bars: 10 μm. **(c)** Quantification of (a) and (b) comparing the integrated density (IntDens) of ErbB4 fluorescence signals of control and *Dnmt1*-KD MGEs. Unpaired, two-tailed Student's *t*-test with subsequent Welch's correction, $p < 0.001$ *** ($n = 88$ cells for control siRNA and 78 cells for *Dnmt1* siRNA, $N = 4$ experiments). **(d-f)** Live-cell imaging analysis of *Sst-Cre/tdTomato* and *Sst-Cre/tdTomato/Dnmt1 loxP*^{2} cells in E14.5 organotypic brain slices (350 μm coronal sections, time-period of imaging: 20 h). Analysis of the migrated path length and the radial migration velocity are shown in **(d)** and **(e)**, respectively. **(f)** DNMT1 does not impact the migratory morphology of tdTomato-positive cells investigated in organotypic brain slices (350 μm coronal sections). Two-tailed nested *t*-test ($p < 0.01$ **) with $N = 3$ embryos and $n = 4$ slices for control and KO animals respectively, $n = 185$ cells for control, and $n = 219$ KO cells. **(g-i)** siRNA-mediated depletion of *Dnmt1* in MGE-derived single cells *in vitro* (E14.5 + 1div) does not affect the cellular morphology compared to control siRNA-transfected cells. Scale bars: 10 μm. Quantification is shown in **(i)**. Unpaired, two-tailed Student's *t*-test with subsequent Welsh's correction, $n = 60$ cells each for control siRNA and *Dnmt1* siRNA. siRNA: small-interfering RNA; LP: leading process, n.s.: not significant.

Extended Data Figure E7:

The cortical size and dimensions of its different regions do not differ between E14.5 *Sst-Cre/tdTomato/Dnmt1-loxP²* and E14.5 *Sst-Cre/tdTomato* brains. **(a)** Schematic illustration of the regions and extensions measured to analyze cortical extensions and areas of coronal, 50-*µ*m-thick, fixated slices. Respective quantifications are depicted in **(b)** and **(c)**. Two-tailed nested *t*-test, $N = 3$ embryos for both genotypes, $n = 13$ slices for *Sst-Cre/tdTomato* and $n = 9$ slices for *Sst-Cre/tdTomato/Dnmt1 loxP²*. MZ: marginal zone, IZ: intermediate zone, SVZ+VZ: subventricular and ventricular zone, not significant.

Extended Data Figure E8:

The cortical size and dimensions of its different regions are not different in E16.5 and E18.5 *Sst-Cre/tdTomato/Dnmt1 loxP²* embryos compared to age-matched *Sst-Cre/tdTomato* individuals. **(a, d)** Schematic illustration of the regions and extensions measured to analyze cortical dimensions and areas of coronal, 50-*µ*m-thick, fixated slices at E16.5 **(a)** and E18.5 **(d)**. Respective quantifications are depicted in **(b)**, **(c),** and **(e)**. **(b and c)** Quantification of the cortical dimension of embryos at E16.5. Unpaired nested *t*-test, $N = 4$ embryos for both genotypes, $n = 12$ slices for *Sst-Cre/tdTomato,* and $n = 15$ slices for *Sst-Cre/tdTomato/Dnmt1 loxP²*. **(e)** Quantification of the cortical dimension of embryos at E18.5. Unpaired nested *t*-test, $N = 4$ embryos for both genotypes, $n = 12$ slices for *Sst-Cre/tdTomato,* and $n = 9$ slices for *Sst-Cre/tdTomato/Dnmt1 loxP²*. MZ: marginal zone, CP: cortical plate, IZ: intermediate zone, SVZ+VZ: subventricular zone, n.s.: not significant.

Extended Data Figure E9:

TdTomato-expressing cells show immunoreactivity for neuropeptide Y and calretinin. Exemplary microphotographs of sagittal sections from a four-month-old *Sst-Cre/tdTomato* animal (Bregma 2.76). **(a** and **b)** Examples of immunohistochemical stainings using an anti-somatostatin antibody (green) and an anti-neuropeptide Y antibody (NPY, magenta). TdTomato-positive cells are depicted in red. **(c** and **d)** Examples of immunohistochemical stainings using an anti-somatostatin antibody (green) and an anti-calretinin antibody (magenta). TdTomato-positive cells are depicted in red. Scale bars in **(a)** and **(c)**: 100 µm. Scale bars in **(b)** and **(d)**: 20 µm (magnified views of sections outlined in **(a)** and **(c)**, respectively). **(e)** Mammalian phenotype ontology analysis for the enrichment of the genes upregulated in *Sst-Cre/tdTomato/Dnmt1 loxP²* animals at E14.5. ShinyGO 0.80, Curated.MGI pathway database.

Extended Data Figures

Extended Data Figure E1

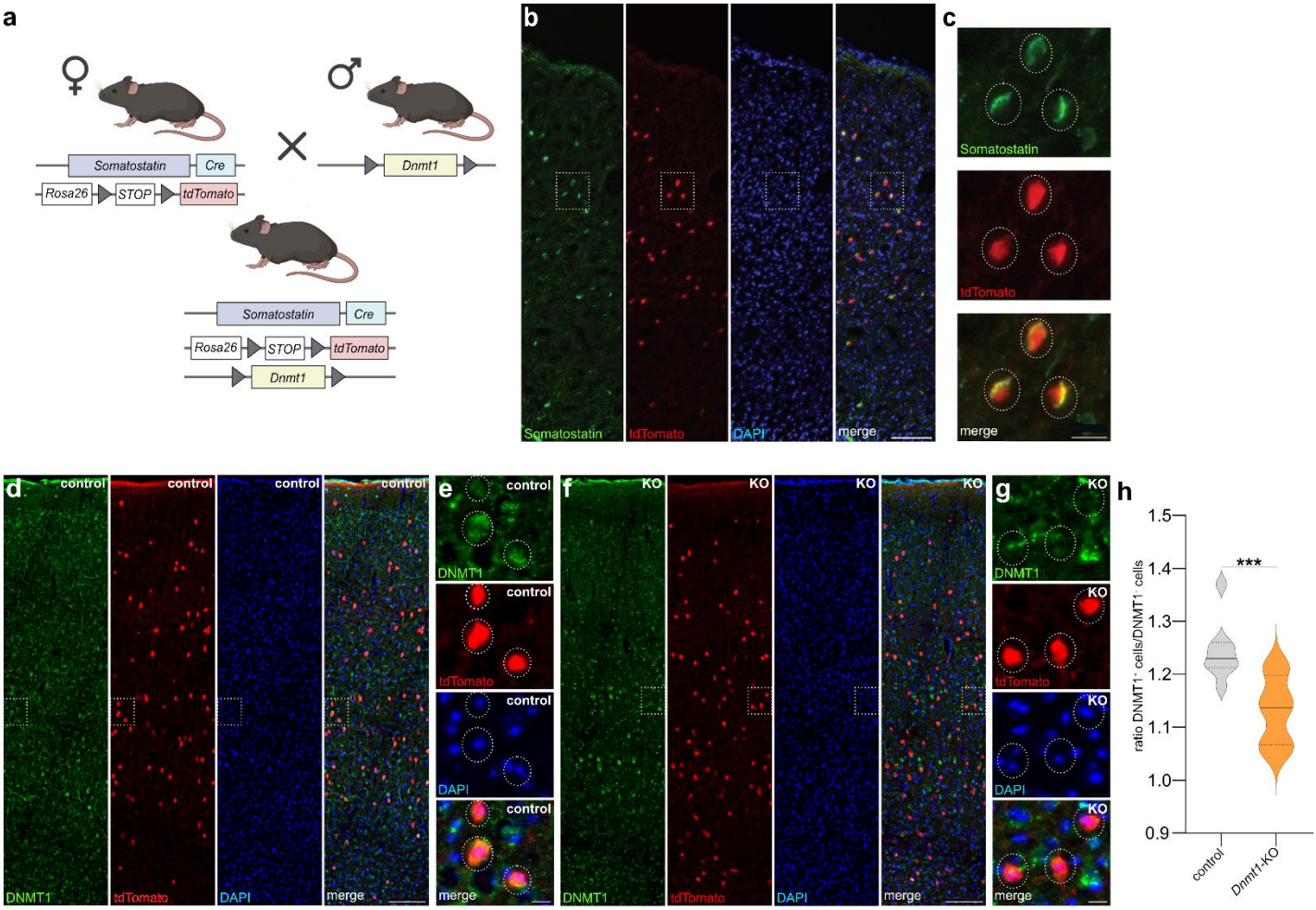

Extended Data Figure E2

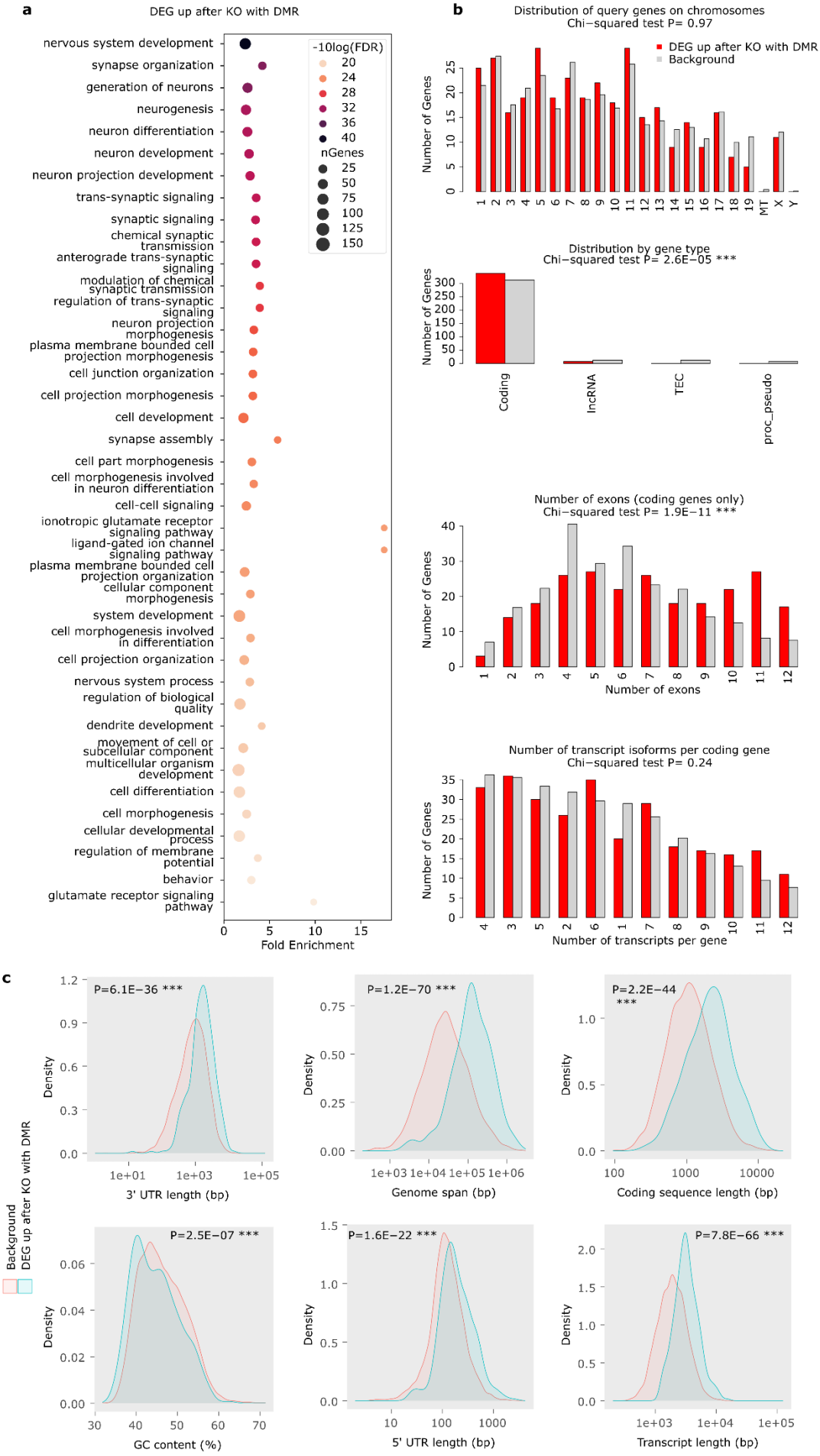

Extended Data Figure E3

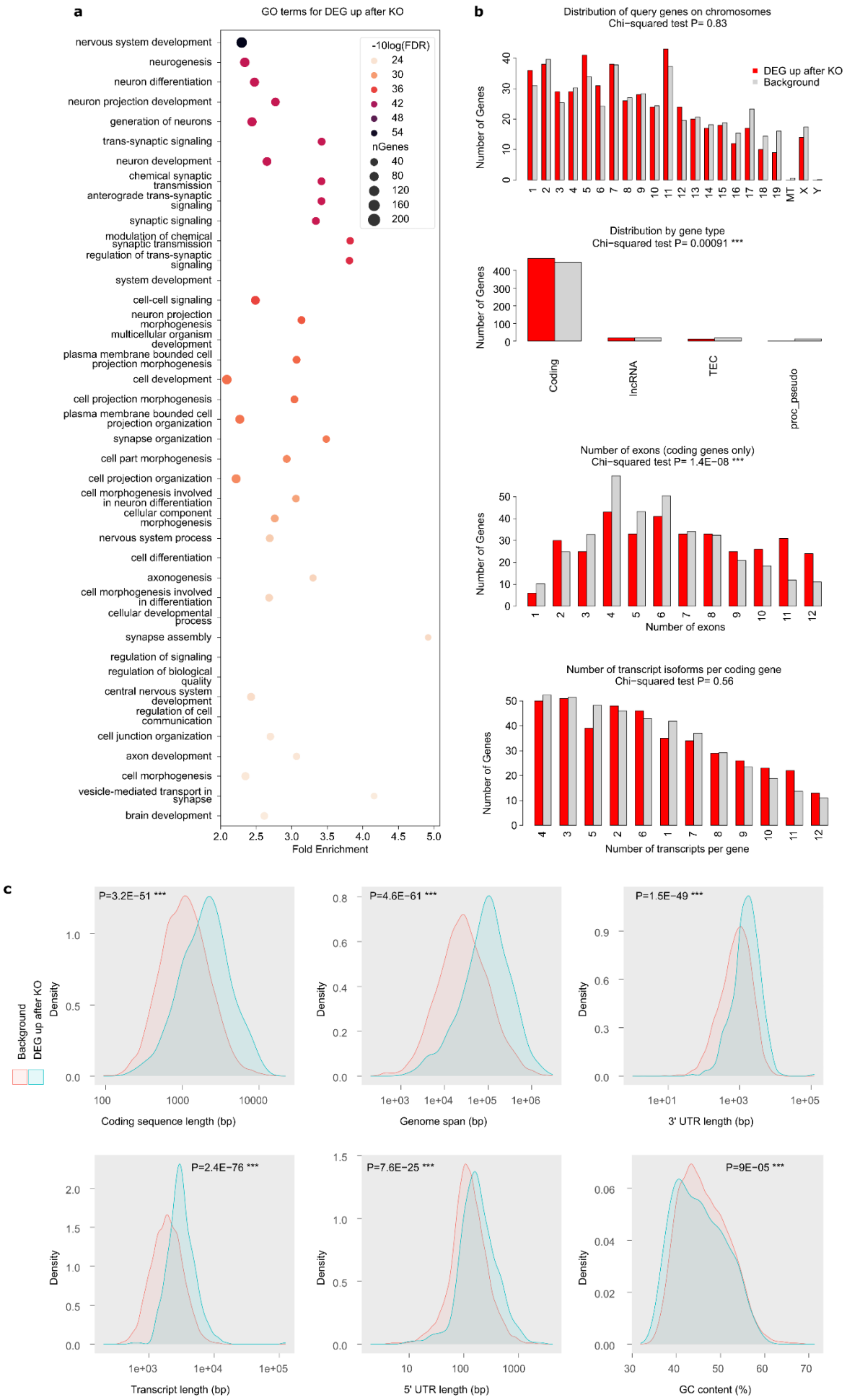

Extended Data Figure E4

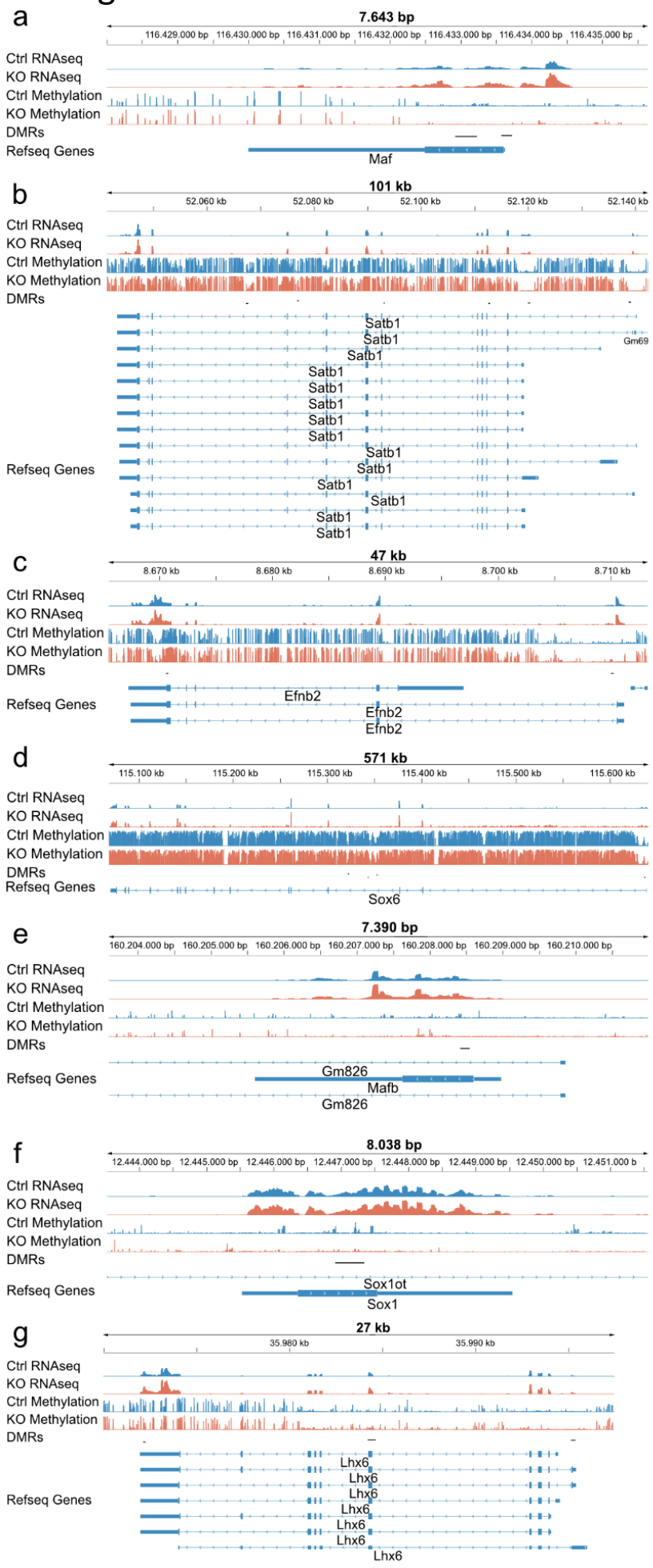

Extended Data Figure E5

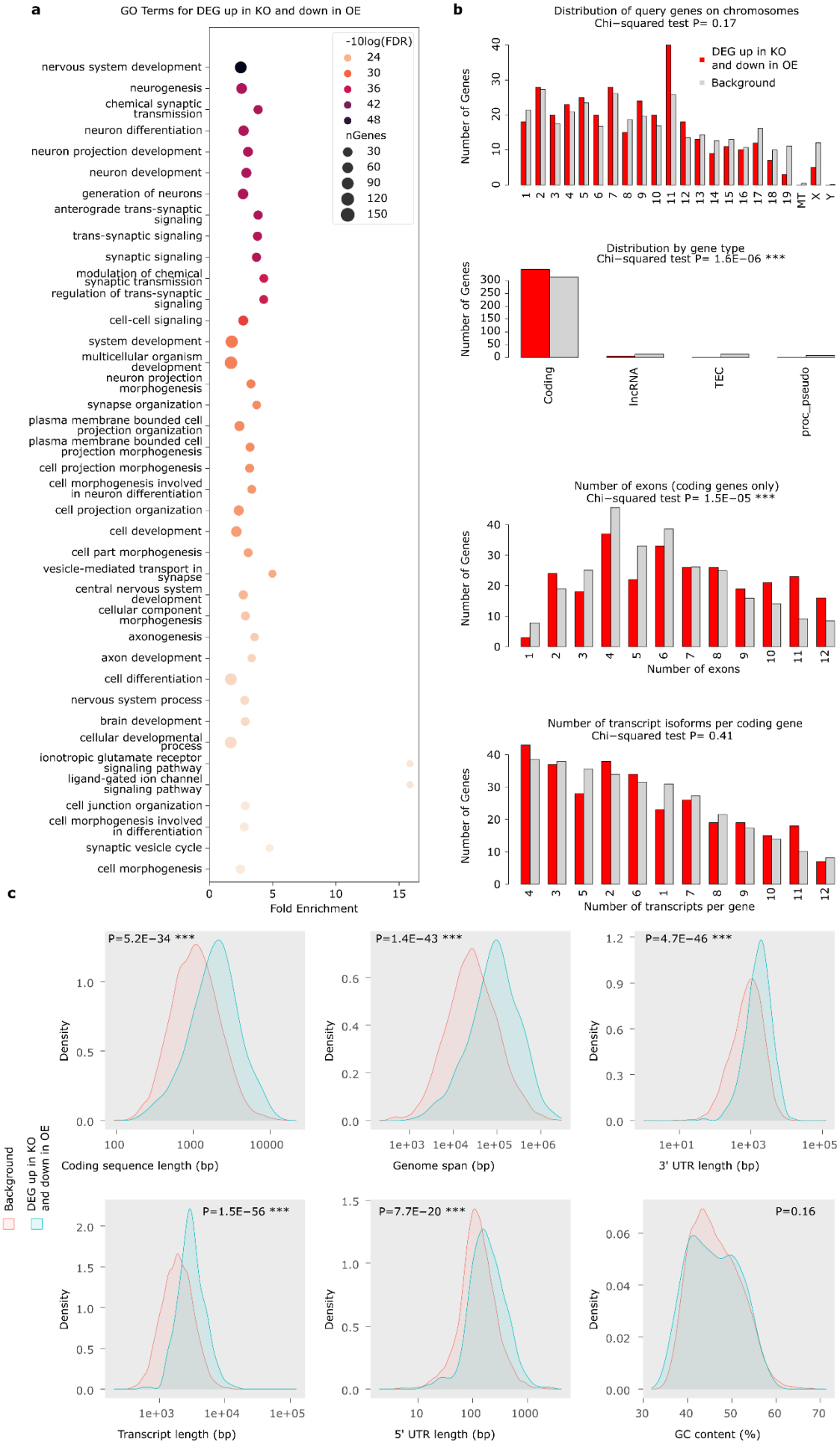

Extended Data Figure E6

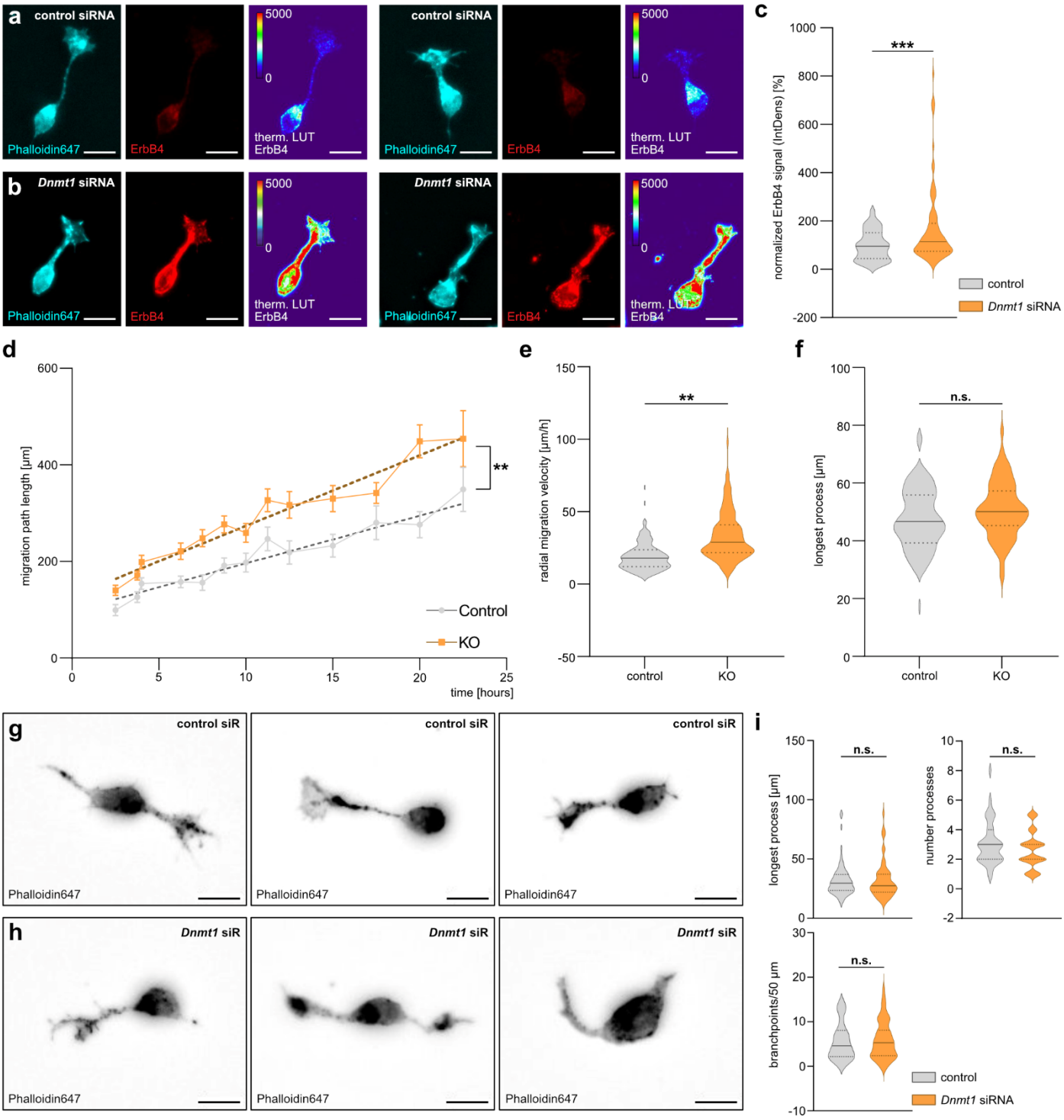

Extended Data Figure E7

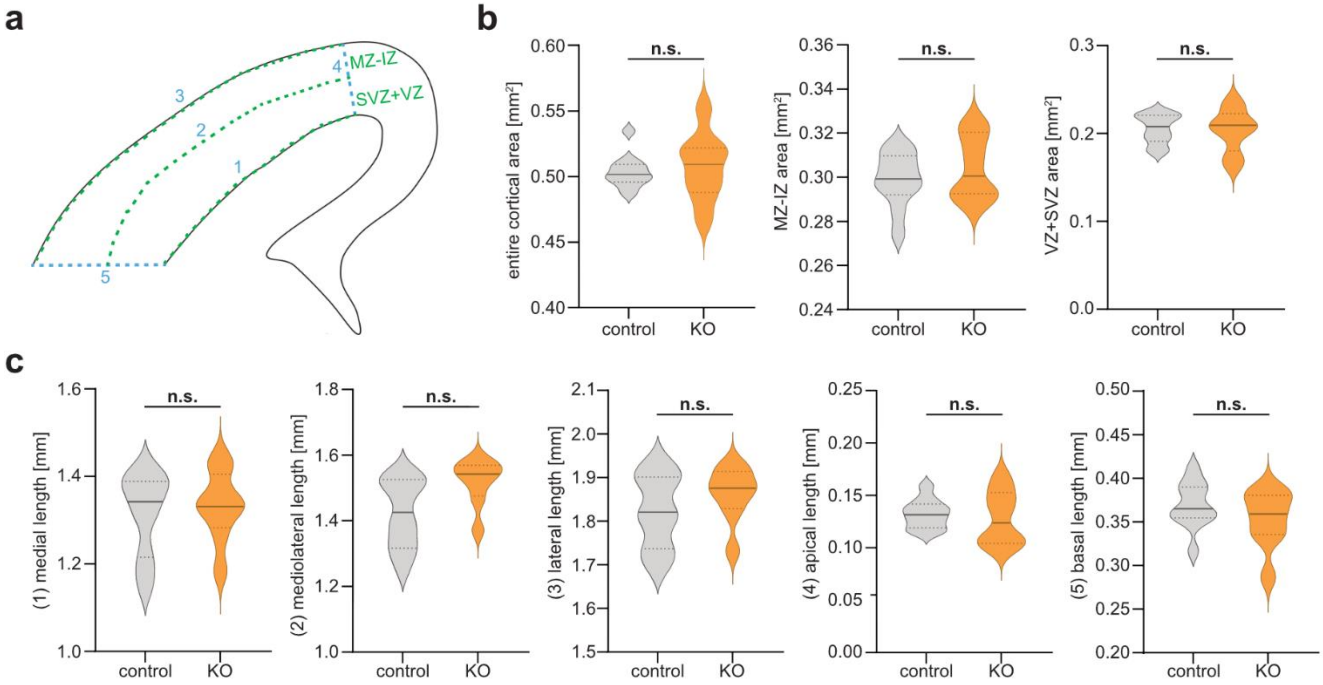

Extended Data Figure E8

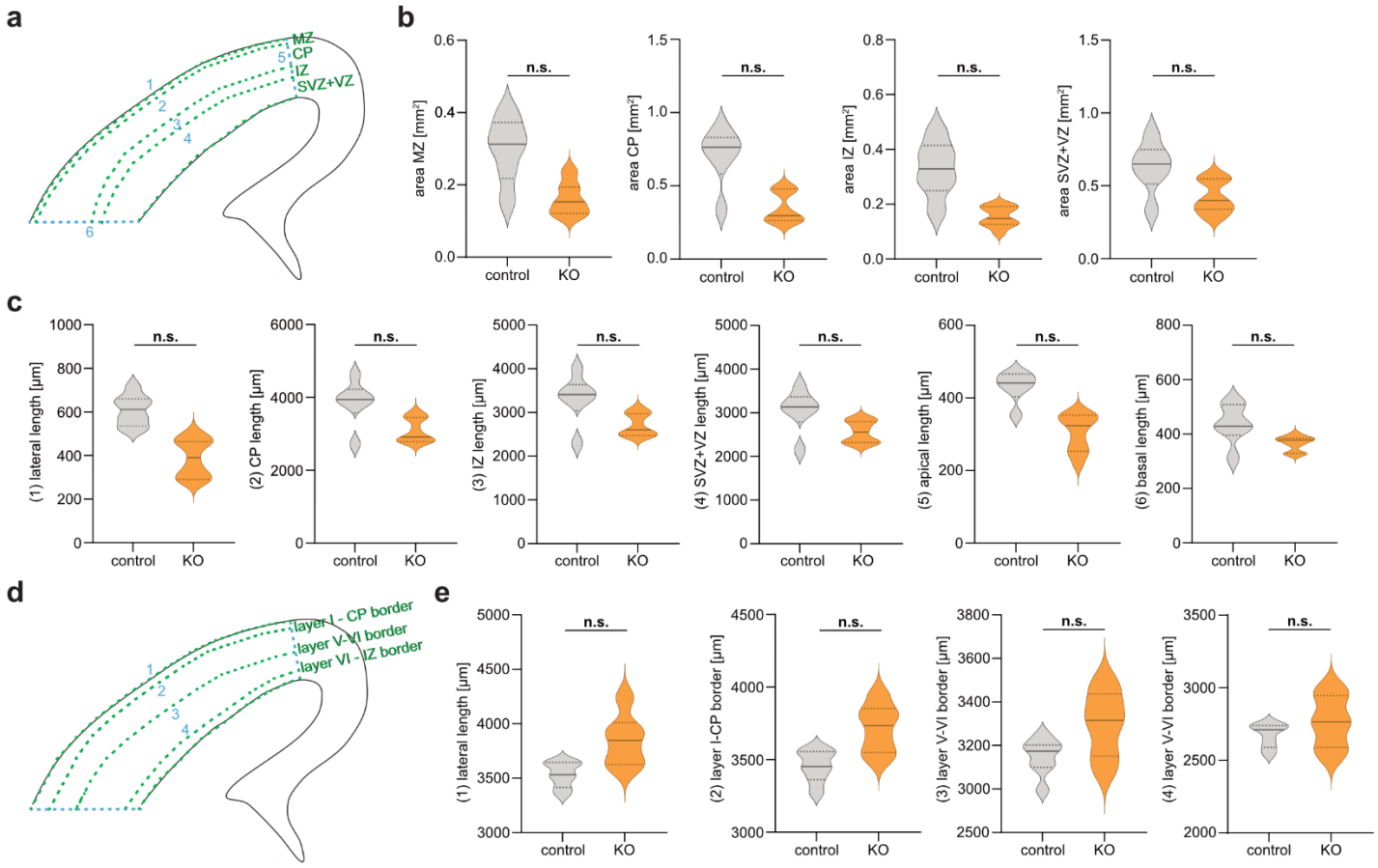
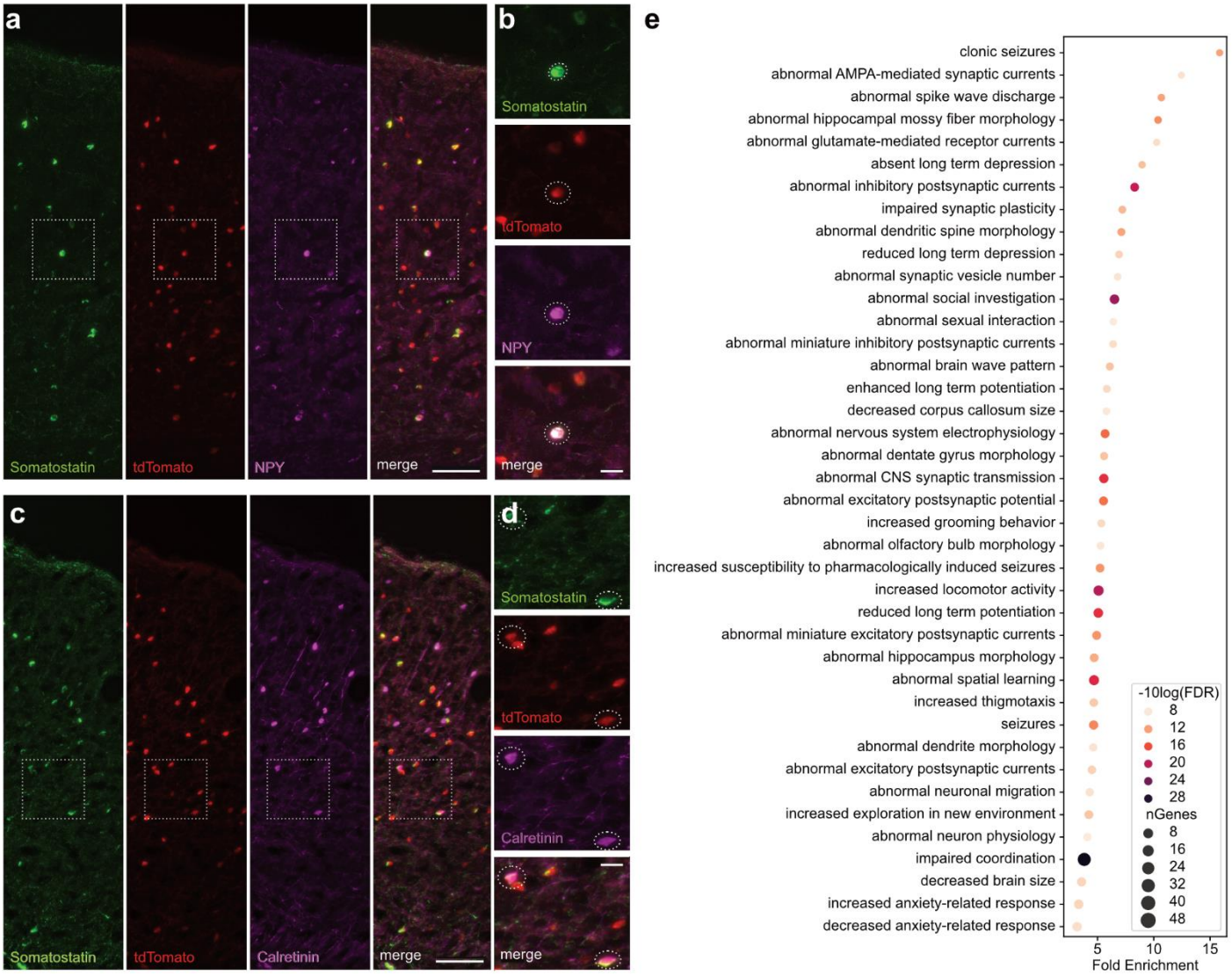
Extended Data Figure E9